Journal of Materials Chemistry C

Accepted Manuscript

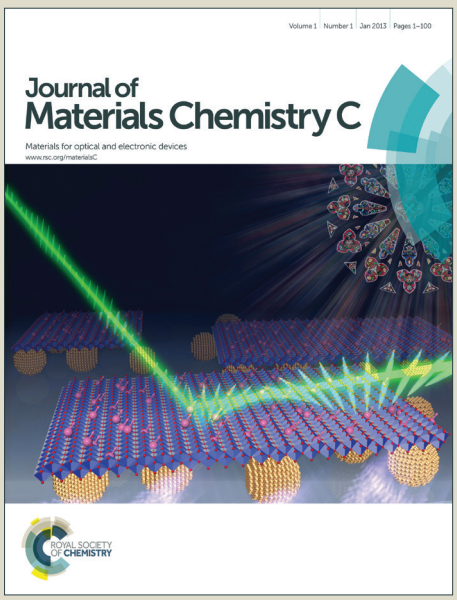

ROYAL SOCIETY OF CHEMISTRY

www.rsc.org/materialsC

Recent Development of Core-Shell SnO_2 Nanostructures and Their Potential Applications

Arik Kar[#] and Amitava Patra*

Department of Materials Science, Indian Association for the Cultivation of Science, Kolkata 700032, India

Abstract

This feature article highlights the recent development of core-shell SnO_2 nanostructures for their potential applications, i.e. optical, electrical, photo-electrochemical, photo-catalytic and gas sensing. Current studies reveal that the core-shell SnO_2 nanocrystals could pave the way for developing new challenging devices because core-shell structures exhibit significant improvement of different physical properties e.g. electrical, optical, and electrochemical etc. Here, we mainly highlight the impacts of core-shell structures of SnO_2 nanocrystals on optical, electrical, photo-electrochemical, photo-catalytic and gas sensing properties. To begin with, we illustrate general synthetic methodologies for preparing core-shell SnO_2 nanostructures and describe the structural changes due to formation of core-shell nanocrystals. Successively, we emphasize on the fundamental understanding of free charge carrier generation, charge transfer, charge separation, and interfacial charge transfer of the core-shell structures. The chemical and electronic mechanisms for SnO_2 sensor performance have been discussed. We discuss a general analysis of the band structure of the heterojunction formed between SnO_2 core and shell materials. Recent findings reveal that the photoelectrochemical, photocatalytic and gas sensing are increased manifold in core-shell SnO_2 nanocrystals. Finally an outlook on the prospects of this research field is given.

[#] Present address: Department of Chemistry, University of Cambridge, UK

[*]Author to whom correspondence should be addressed; electronic mail:**msap@iacs.res.in**

Phone: (91)-33-2473-4971, Fax: (91)-33-2473-2805

Contents

1. Introduction

Tin oxide (SnO_2) is an important metal-oxide, n-type wide band gap (3.6 eV at 300 K) semiconductor.[1-3] On account of its outstanding electrical, optical, and electrochemical properties, SnO_2 offers a wide range of applications in solar cells,[4,5] catalytic support materials,[6] transparent electrodes,[7,8] and solid-state chemical sensors.[9-13] These unique properties have enthused to design new synthetic methodologies for well-controlled SnO_2 nanostructures. There are numerous synthesis methods available in the literature such as discharge[14], laser ablation[15], solution[16], vapor-liquid-solid (VLS)[17], sol-gel[18], hydro(solvo)thermal[19-22], microwave[1] etc. to prepare various morphological SnO_2 such as nanoparticles[23], nanorods[24], nanodisks[25], nanosheets[26], nanobelts[27], nanowires[28] etc. It is evident that SnO_2 is one of the most important and extensively used metal oxide semiconductor materials for gas sensors due to its high sensitivity and low cost. Over the past decades, significant attention has been paid on enhancing the sensing performance of SnO_2-based gas sensor.[29-32] Again, SnO_2 also finds application as photocatalytic materials.[33] However, it is found that pure SnO_2 have some limitations owing to its low surface area and low stability.[3] To combat with these problems, fabrication of core-shell structures of SnO_2 is found to be prospective.

Core-shell structures of SnO_2 are found to be promising materials to improve the performance of various SnO_2-based devices. The photocatalytic activities of SnO_2 are found to be increased when core-shell structures are formed due to efficient charge separation. There are a number of studies associated to improve the photocatalytic activity of core-shell structured SnO_2 such as SnO_2/TiO_2[34], SnO_2/ZnO[35], SnO_2/CdS[36] etc. It is found that the appropriate shell materials would be served as additional electron sources that can significantly improve the electron conduction in SnO_2 which improves the gas-sensing response.[31] Again, coupling SnO_2 (large bandgap 3.6 eV) with another smaller bandgap semiconductor also facilitates the charge separation by accumulating electrons and holes in separate particles which will enhance the photo electrochemical properties of SnO_2.[37-41]

A few review articles are in the literature on the gas-sensing applications of SnO_2.[42,43] Göpel et al.[42] have mainly focus on the development of SnO_2 nanostructures for gas sensing. Ma et al.[43] wrote a mini-review on various aspects on the performances of SnO_2-based gas sensors. Batzill et al.[44] have highlighted the gas sensing properties of SnO_2 and their controlling factors. There are few review articles on the photoelectrochemistry of transparent SnO_2[45], synthesis and

applications of one-dimensional SnO_2 nanostructures[46], solar cells application of SnO_2:F films[47] and synthesis and applications of hierarchical SnO_2 nanostructures.[48] Interestingly, there is no review article on the impact of core-shell structures of SnO_2 on their potential applications.

The main focus of this feature article is to address the important questions: how the core-shell structures of SnO_2 nanocrystals influence on optical and electrical, photo-electrochemical, photo-catalytic and gas sensing properties. To begin with, we describe the general synthetic methodologies to prepare core-shell structure of SnO_2. Spectroscopic and microscopic methods are being used to understand the structural changes due to core-shell structure which eventually influence the physical properties of SnO_2. We describe the mechanism how core-shell structures improve the electrical, optical, sensing and other physical properties? Finally, an outlook on the prospects of this research field is given.

2. General synthetic methods for preparing core-shell structures of SnO_2 nanocrystals

The synthesis of core-shell nanocrystals is typically classified into two major categories: "top-down" and "bottom-up".[49] The bottom-up approach has proven more appropriate for the synthesis of core-shell nanocrystals. The most vital step during the synthesis of core-shell nanoparticles is to maintain uniform coating and to control the shell thickness. Core-shell nanoparticles are typically synthesized using a two-step process, the synthesis of core is the first step and the synthesis of the shell is the second step. The synthesis techniques of core-shell nanoparticles can be classified into two types:

(i) The core particles are synthesized first and then shell is formed by surface modification;[50-52]

(ii) The core particles are synthesized in situ which is followed by surface coating;[53,54] In this method, the core particles are synthesized first using appropriate reactants in the presence of a surface modifier; then more reactants are added to form the shell in situ.[55] Shell material is selectively deposited on the modified core surface and core-shell particles are formed. The main disadvantage of this process is that impurities may be trapped between the core and shell layer.

Temperature is the most important reaction parameter which is being used to control the reaction kinetics for core-shell nanoparticle formation. The working temperature range depends mostly on the reaction mechanism of core or shell formation. In general, a low temperature is favorable for core-shell nanoparticle synthesis.[49] The proper band alignment and small lattice mismatch between shell and core are the important parameters for choosing core and shell materials.[49] Due to lattice mismatch, lattice strain will develop which will produce surface

defects in the interface. Cozzoli et al.[56] have reported the influence of interfacial energy on core-shell structure formation. It is recommended to choose shell materials with less lattice mismatch with the core.

In view of SnO_2-based core-shell nanoparticles, significant efforts have been devoted in the last decade to synthesize high quality SnO_2-based core-shell nanoparticles. The chemical and the physical properties of core-shell SnO_2 nanostructures depend on the nature of the shell. There are few techniques that can be taken care for the formation of uniform shell over SnO_2 core nanoparticles. The techniques are (i) sequential addition of the reactants, (ii) proper choice of the shell forming agent, (iii) control over the rate of addition of the shell forming agent, (iv) control the reaction temperature and (v) the appropriate selection of organic ligands adhered to the surface of core. There are different chemical synthesis methods available in the literature such as hydrothermal, sonochemical, colloidal, chemical vapor deposition etc. to prepare core-shell SnO_2 nanocrystals.[36,57-60] In this section, we briefly discuss some of the current methods for preparing various core-shell structures of SnO_2 nanocrystals.

2.1. Hydrothermal method

This is an outstanding method for generating core-shell nanocrystals with controlled crystal sizes and good dispersibility in solutions. It refers to a chemical synthesis procedure within a sealed autoclave environment under high pressure and temperature (often above the critical point of the solvent). Hydrothermal method is being used for the synthesis of SnO_2-based core-shell nanoparticles.[36,57] Patra et al.[36] have used this method for the synthesis of core-shell SnO_2/CdS nanorods by using a single-source precursor cadmium thiobenzoate complex for the CdS shell. They have modified the surface of SnO_2 nanorods by cetyl trimethyl ammonium bromide (CTAB) using ultrasonic irradiation. The detail synthetic procedure is represented in fig. 1a. The TEM image of as-prepared sample is also given inset of fig. 1a. The main advantage of this synthetic method is the use of single source precursor for the CdS shell. The surface capping agent CTAB is being used for creating uniform shell thickness. Fan et al.[57] have used a hydrothermal process for the fabrication of ZnO nanostructures hierarchically assembled on SnO_2 nanowire backbones. Firstly, the SnO_2 nanowires were coated with ZnO nanoparticles as seeds by a dip-coating technique. Then, the SnO_2 nanowire covered substrates were immersed into an aqueous solution of zinc nitrate ($Zn(NO_3)_2 \cdot 6H_2O$) and hexamethylenetetramine ($C_6H_{12}N_4$). The main advantage of this synthetic technique is that the morphology of ZnO shell

can be tuned by adjusting the salt concentration, reaction time, and additives. Zhang et al.[58] have reported an innovative hydrothermal shell-by-shell templating strategy appropriate for the preparation of SnO_2 rattle-type nanospheres. First, they have used an organic capping agent (PVP) to anchor the SiO_2 nanoparticles and prevent the aggregation of nanoparticles in solution. Then, the SnO_2 nanospheres were coated with silica and used as templates to prepare SnO_2 rattle-type nanospheres. The fabrication process is a three-step procedure, and each step is well controlled (fig. 1b). Peng et al.[34] have used a hydrothermal process for the synthesis of TiO_2 coated SnO_2 nanotubes with different SnO_2 contents. It is clear from the above discussion that the hydrothermal method is an effective approach for the synthesis of SnO_2-based core-shell nanoparticles.

2.2. Sonochemical method

An alternative approach for the formation of SnO_2-based core-shell nanoparticles is the sonochemical synthesis by employing acoustic waves. In this method, the required amount of SnO_2 core materials is taken in an appropriate solvent and sonicated. After sonication, the required amount of shell forming agent was added to form core-shell nanostructures. The ultrasound helps to initiate reaction leading to growth of shell and disperse the nanoparticles in solution. Gao et al.[59] have used a simple sonochemical approach for the preparation of SnO_2 /CdS core-shell heterostructures. They have prepared SnO_2 core particles by thermal evaporation of metallic Sn powders. Then, cadmium chloride and thiourea were added to water in a sonication cell and the reaction mixture was irradiated with a high-intensity ultrasonication (100W, 40 kHz). Argon gas was bubbled through the reaction mixture prior to the sonication to expel dissolved oxygen. This method is an effective approach for the synthesis of SnO_2-based core-shell nanoparticles.

2.3. Colloidal method

Another approach for the synthesis of SnO_2-based core-shell nanoparticles is the colloidal synthesis. This method requires three components: core and shell precursors, organic surfactants and solvents.[61] Upon heating the reaction mixtures to a sufficiently high temperature, the precursors chemically transform into active atomic or molecular species followed by formation of core-shell nanocrystals whose subsequent growth is greatly affected by the presence of surfactant molecules. The advantages of this method include large-scale production, safe, convenient, energy efficient etc. Kamat et al.[60] have synthesized CdS-capped SnO_2 colloids in

aqueous medium and this method involves the adsorption of Cd^{2+} ions on to the interior core of SnO_2 followed by the exposure of the solution to H_2S. The as-prepared CdS-capped SnO_2 colloids was found to be stable for several days. Again, it is possible to vary the thickness of the CdS shell by controlling the concentration of Cd^{2+}. A simple two-step colloidal method has been used by Li et al.[62] for the preparation of ZnS coated SnO_2 nanowires. Initially, SnO_2 core particles are immersed in Na_2S solution for a certain time. Then, the samples are immersed in $Zn(NO_3)_2$ solution for the same time. The thickness of ZnS shell is also tuned by controlling the amount of shell precursor and deposition time.

2.4. Chemical vapor deposition

Chemical vapor deposition (CVD) is being used to produce high-purity, high-performance core-shell materials. In typical CVD, the wafer (substrate) is exposed to one or more volatile precursors, which react and/or decompose on the substrate surface to produce the desired deposit. The advantages of this technique are (i) uniform distribution over large areas, (ii) no compositional gradients across substrate, (iii) more selective area deposition because of higher activation energy for reaction with foreign substances. Mathur et al.[63] have used two-step chemical vapor deposition (CVD) in combination with metal-catalyzed vapor-liquid-solid (VLS) growth mechanism as a new approach to synthesize TiO_2 coated SnO_2 nanowires. They have utilized the $Sn(O^tBu)_4$ and $Ti(O^iPr)_4$ complex in the CVD process. The thickness of TiO_2 shell was adjusted by controlling the precursor flux and deposition time. Kim et al.[32] have fabricated core-shell SnO_2/ZnO nanofibers by means of a novel two-step process. First, SnO_2 core nanofibers were synthesized by electrospinning. Sequentially, ZnO shell layers were grown using CVD with a controlled manner on the core nanofibers. Hotchandani et al.[64] have developed a photo-electrochemical cell coupled with SnO_2/CdSe nanocrystalline semiconductor electrode which has been prepared by sequential deposition of SnO_2 and CdSe films onto an optically transparent electrode. The disadvantages of CVD technique are (i) safety and contamination, (ii) hydrides and carbonyls are poisonous, (iii) high cost chemicals. There are also extensive reports in the literature for the synthesis of SnO_2-based core-shell heterostructures.[65-74] We briefly summarize some of the recent reports in Table 1. Analysis suggests that several attempts are made to control the thickness and uniform shell of core-shell materials.

3. Physical properties of core-shell structures

3.1. Structural information

A large number of characterization techniques have been used to get structural information of SnO_2-based core-shell nanostructures. Among these techniques, X-ray diffraction (XRD), transmission electron microscopy (TEM), Furrier transformed infrared spectroscopy (FTIR), Raman spectroscopy and X-ray photoelectron spectroscopy (XPS) techniques are frequently being used to recognize the structural changes due to formation of core-shell structures. In this section, we will discuss some of the characterization techniques.

3.1.1. X-ray diffraction (XRD) technique

There is a significant change in the XRD pattern of SnO_2 nanocrystals after formation of core-shell structures. Core-shell structures play significant role on tuning the cell parameters which would influence on physical properties. There are numerous reports in the literature where considerable changes are reported in the XRD pattern after formation of core-shell structures of SnO_2.[32,36,63] Patra et al.[36] have found some remarkable changes after surface coating of SnO_2 nanorods with CdS nanoparticles. Figure 2a revealed the XRD patterns of pure SnO_2 nanorods, pure CdS nanoparticles, a physical mixture of CdS and SnO_2 nanocrystals and core-shell SnO_2/CdS nanorods. Tetragonal phase of SnO_2 and cubic phase of CdS are observed while core-shell SnO_2/CdS nanorods showed the peaks at 30.74^o (200), 44.24^o (220) and 71.62^o (331), indicating the existence of cubic phase of CdS along with the tetragonal phase of SnO_2. It is found that the cell parameters cell parameters are modified due to core-shell structures, indicating the structural change occurs. Kim et al.[32] have confirmed the formation of ZnO shell layers on core SnO_2 nanofibers. Mathur et al.[63] have observed the rutile phase of SnO_2 and no other peak of TiO_2, indicating the amorphous nature of the TiO_2 layer. Li et al.[62] have observed the tetragonal rutile structure of SnO_2 and wurtzite structure of ZnS appear with increasing the thickness with time in ZnS coated SnO_2 nanowires. Gao et al.[72] have designed a competent core-shell SnO_2-TiO_2 for dye-sensitized solar cell. They have observed that all the diffraction peaks of SnO_2 can be well indexed to a rutile structure of SnO_2. The shifting of diffraction peaks to larger angles in core-shell structure is observed due to modification of the lattice constant.[50] Zhong et al.[75] have also observed the shift of diffraction peaks to larger angles located between the cubic CdTe and CdS phase in CdTe/CdS core-shell nanocrystals. Analogous changes in the diffraction pattern are also reported[76-78] for previous core-shell nanostructures.[79] Kar et al.[36] have confirmed

the formation of CdS shell on SnO_2 nanorod by XRD investigation and figure 2b illustrates the XRD patterns of pure SnO_2 nanorods and the as-prepared core-shell SnO_2/CdS nanorods. The diffraction peaks are shifted to larger angles for the core-shell heterostructure, which confirms the formation of core-shell structures. In reality, the diffraction peaks shift to larger angles in the core-shell heterostructure owing to smaller lattice constant for core-shell SnO_2/CdS nanorods compared with pure SnO_2 nanorods. XRD analysis reveals the core-shell structures modify the crystal phase, crystal size and cell parameters which certainly have enormous influence on their physical properties.

3.1.2. Transmission electron microscopy (TEM)

Formation of SnO_2-based core-shell structure can also be confirmed by TEM and high resolution transmission electron microscopy (HRTEM) investigation. TEM provides important information regarding particle size, core size, shell thickness, uniform or nonuniform shell coating, etc. HRTEM images provide information on crystallinity, lattice fringes and d-spacing of the core-shell materials. An elemental mapping and line scan EDS analysis also confirm the formation of shell over core particle. Patra et al.[36] have used TEM and HRTEM study to confirm the formation of CdS shell over SnO_2 core (fig. 2c). Fig. 2c(i) show the TEM image of SnO_2 nanorods which are almost uniform in size and shape. From the HRTEM image of a single SnO_2 nanorod (fig. 2c(ii)), the observed distance between lattice planes (0.335 nm) which corresponds to (110) plane of tetragonal phase of SnO_2. Figure 2c (iii) shows the successful deposition of CdS nanoparticles on SnO_2 nanorods. The measured distance between lattice plane is 0.341 nm from HRTEM image of the deposited CdS nanoparticles [fig. 2c(iv)], which is well matched to the reported value for the (111) plane of the cubic CdS. An elemental mapping and line scan EDS analysis confirm the formation of CdS shell over SnO_2 nanorods which are given in figs. 2c (v-xvi). Kim et al.[32] have confirmed the formation of core-shell SnO_2/ZnO by using TEM investigation. From high-resolution TEM image of a ZnO shell layer, the 0.52 nm d-spacing confirming the formation of ZnO shell layers over SnO_2. They have further observed that Zn is localized in the outer surface of the nanofiber in contrast with Sn which is localized in the interior of the nanofiber, demonstrating the formation of core-shell SnO_2/ZnO nanofibers. EDS elemental mapping measurements confirm the well-defined spatial distribution of Zn, O, and Sn. The formation of MoO_3 coated SnO_2 nanobelts by TEM and HRTEM analysis is confirmed by Chen et al.[74] The hierarchical assembly of ZnO nanostructures on SnO_2 backbone nanowires by

using TEM and HRTEM techniques has been confirmed by Fan et al.[57] It is evident that the TEM and HRTEM analysis confirms the core-shell structures of SnO_2.

3.1.3. FTIR and Raman spectroscopy

Infrared spectroscopy and Raman spectroscopy are used to study vibrational, rotational, and other low-frequency modes. These two spectroscopic techniques are frequently being used to understand the structural changes of SnO_2 after core-shell formation. Wu et al.[67] have investigated the interaction between polypyrrole and SnO_2 hollow spheres by FTIR study and the observed reduced peak intensity is due to appearance of Sn-O-Sn band. The reduced peak intensity is attributed to the interaction between polypyrrole and SnO_2 hollow spheres. Kim et al.[70] have investigated the formation of the In_2O_3 shell over SnO_2 by Raman spectrum and they have observed three normal phonon modes E_g, A_{1g}, and B_{2g} at 474, 629, and 772 cm^{-1}, respectively due to polycrystalline SnO_2 with a tetragonal structure. In addition to these classical modes, three weak Raman shifts at 238, 306, and 707 cm^{-1} were observed which are attributed to the presence of cubic In_2O_3. Li et al.[62] have established tetragonal rutile SnO_2 phase in core-shell SnO_2/ZnS nanowires by Raman spectroscopy. They have assigned the Raman peaks at 473, 519, 634, and 773 cm^{-1} as E_g, A_{2u}, A_{1g}, and B_{2g} modes, respectively. After the SnO_2 core is modified by the ZnS shell, new lines at 696 cm^{-1} and a low-energy shoulder of 634 cm^{-1} has been observed with a red shift of the 519 cm^{-1} line to 500 cm^{-1}. The appearance of the new lines in core-shell sample is attributed to the surface optical phonon modes, which mainly originate from the modification of the crystallographic structure of the ZnS shell and the reconstruction of the SnO_2/ZnS interface. Thus, FTIR and Raman spectroscopic techniques are very useful for analysis the core-shell structures.

3.1.4. X-ray photoelectron spectroscopy (XPS) technique

X-ray photoelectron spectroscopy (XPS) technique can be reasonably used if the thickness of the shell is in between 3-6 Å.[80] The binding force between SnO_2 core with shell material can be analyzed by XPS. Yang et al.[81] have analyzed the binding force between the SnO_2 core and the ZnO shell with the help of this technique. The presence of Sn-O-Zn bonds between SnO_2 core and the ZnO shell is evidenced by the comparison of the Sn $3d_{5/2}$ spectra of the core-shell material and the pure SnO_2. It is obtained that the Sn $3d_{5/2}$ peak is shifted to a lower energy for the core-shell material (486.20 eV) from that of the pure SnO_2 (486.65 eV), indicating the ZnO shell formation on SnO_2 nanoparticles. Core-shell SnO_2/ZnO heterojunction

photocatalysts have been successfully prepared by Toupance et al.[82] using a two-step solution route. Liu et al.[68] have investigated the chemical composition and the binding energy of core-shell SnO_2/TiO_2 heterostructures by XPS analysis. The fully scanned spectra demonstrate that Ti, O, and C elements exist in bare TiO_2, while Ti, Sn, O, and C exist in core-shell SnO_2/TiO_2 heterostructures, respectively. The splitting of the 3d doublet of Sn is 8.5 eV which indicates the valence state of Sn is +4. Again, Wang et al.[83] have confirmed the chemical composition and the binding force between core and shell of highly porous core-shell SnO_2/TiO_2 nanofibers by XPS method. The splitting between Ti $2p_{1/2}$ and Ti $2p_{3/2}$ is 5.7 eV, indicating the normal state of Ti^{4+} exists in the SnO_2/TiO_2 nanofibers. No shifts of the peaks for Ti 2p confirm the unchange structure of TiO_2 after formation of core-shell SnO_2/TiO_2 nanofibers. Qiao et al.[84] have investigated the elemental composition and the binding force of SnO_2@C spheres. A dominant peak (284.4 eV) is due to the existence of elemental carbon is observed and the peak (286.5 eV) indicates the presence of C-O bonds. In SnO_2 nanobelt/ZnO core-shell, the Sn $3d_{5/2}$ and Zn $2p_{3/2}$ high-resolution spectra with binding energies at 486.7 and 1022.2 eV respectively are observed,[85] which are assigned to Sn^{4+} in SnO_2 and Zn^{2+} in ZnO. The hydrophilic nature of core-shell SnO_2/V_2O_5 nanowires is confirmed by Kang et al.[69] The binding energies of S 2p and O 1s in SnO_2/SnS_2 were observed at about 161.34 and 530.83 eV, respectively, which also suggest the formation of SnS_2 and SnO_2 crystals.[86]The above discussion undoubtedly reveals that shell material plays a significant role on the modification of chemical composition and binding force which eventually influence their optical, electrical, photocatalytic, photoelectrochemical and gas sensing properties.

3.2. Optical and electrical properties

SnO_2 is an n-type semiconductor with a large band gap (Eg = 3.6 eV at 300 K)[1,3] and oxygen vacancies are known to be the most common defects in SnO_2 and usually act as radiative centers in luminescence processes. These oxygen vacancies typically act as deep defect donors in SnO_2 and would cause the formation of new donor levels in the band gap.[1] The photoluminescence (PL) emission of SnO_2 is due to a transition of an electron from a level close to the conduction band edge to a deeply trapped hole in the bulk of the SnO_2 nanocrystals.[87] Enhancement of luminescence (by elimination of non-radiative pathways) of SnO_2 can be achieved by surface coating with another band gap semiconductor material. The choice of shell material is vital for localization of the electron-hole pair. A recent review on core- shell

semiconducting nanocrystals discusses the fundamental properties of core-shell structures of II–VI, IV–VI, and III–V semiconductors.[88] SnO_2 nanocrystals can also be coated with an insulating inorganic shell to enhance the fluorescence. Depending on the shell materials, core-shell SnO_2 nanostructures may be the following three types:

1. Type I - where the band gap of core SnO_2 is smaller than that of the shell. Both the conduction and valence band edges of the core SnO_2 lie within the band gap of the shell, which confines both electrons and holes in the SnO_2 core.
2. Reverse Type I - where the core SnO_2 has a wider band gap than the shell, and the conduction and valence band edges of the shell lie within those of the core SnO_2. The lowest available exciton energy separation occurs when the charge carriers are localized in the shell.
3. Type II - where the valence and conduction band edges of core SnO_2 are both lower and higher than the band edges of the shell. The lowest energy separation of the electron and the hole will occur when the hole is confined in the core SnO_2 valence band and the electron is confined in the shell conduction band.

A few reports about optical property have been found in core-shell structures of SnO_2 nanocrystals.[89,90] Li et al.[62] have reported the optical properties of core-shell SnO_2/ZnS (fig. 3a). A broad emission centered at 370 nm for pure SnO_2 is attributed to the band-acceptor transition.[91-93] A change in the intensity of the PL is observed when SnO_2 is coated by ZnS shell with varying shell thickness. The relative intensity of the samples as a function of ZnS treatment time is presented in the inset of fig. 3a. The increase of PL intensity in the core-shell structures indicates that the ZnS capping greatly reduces the number of surface states of core SnO_2. However, it would passivate most of the dangling bonds on the surface of the SnO_2 core for thick shell by removing the surface states and enhance the PL peak intensity, as shown in fig. 3a. Fan et al.[57] have observed remarkable changes in PL spectra in core-shell SnO_2/ZnO nanostructures because the intensity of defect-related emission from SnO_2 is remarkably suppressed after surface coated by ZnO nanorods. Kar et al.[36] have fabricated core-shell SnO_2/CdS heterostructures and study their decay dynamics by using time resolved photoluminescence study. Figure 3b demonstrates the time resolved photoluminescence (PL) decay curves for SnO_2 nanorod and core-shell SnO_2/CdS nanorod.[36] From the inset plot of figure 3b (PL spectra), it is found that the PL intensity of core-shell SnO_2/CdS nanorod is higher than uncoated SnO_2

nanorods. The decay curves (figure 3b) are well fitted with tri-exponential to obtain the average decay time. The average decay time values are 7.2 ns for pure SnO_2 nanorod and 11.2 ns for core-shell SnO_2/CdS nanorod. The enhancement of average lifetime value (7.2 ns to 11.2 ns) indicates the efficient charge separation occurs in the core-shell structures. The time resolved photoluminescence (PL) decay of the core-shell sample is being used to understand the mechanism and a schematic model is proposed (fig. 3c). In the left side of this model, different relaxation processes in SnO_2 are introduced. In SnO_2, there are three energy levels[87] viz. valence band (VB), defect states and conduction band (CB). Upon photoexcitation, first it creates positive holes in the VB and negative electrons in the CB. The hole in the VB and electron in the CB can radiatively recombine and also the hole in the VB can trap at the oxygen vacancy sites. When the core-shell SnO_2/CdS heterostructure is formed, the mechanism is different (right side of the model). SnO_2 is a direct wide band gap semiconductor while CdS is a short band gap semiconductor (Eg = 2.40 eV at 300 K).[94] The conduction band of CdS (-0.8 V vs. NHE) is also more negative than that of SnO_2 (0.0 V vs. NHE). As a result, upon photoexcitation, the photogenerated electrons of CdS can be transferred to the conduction band of SnO_2, while the holes of SnO_2 can be transferred to the VB of CdS (fig. 3a). Thus, the electron and hole separation becomes prominent in this heterostructure and this effective charge separation leads to longer exciton decay time. Ju et al.[95] have fabricated an efficient white-light-emitting material combining two semiconductors SnO_2 and ZnO. Near-band-edge emission at 375 nm and a defect-related emission band at 600 nm for ZnO[96] are observed whereas SnO_2 shows a broad emission band peaking at 591 nm, which is ascribed to oxygen vacancies.[97] Sun et al.[98] have observed the PL emission from only the secondary-grown ZnO nanostructures, not from the SnO_2 nanobelts which is due to the high-density coverage of ZnO on SnO_2. Kim et al.[99] have investigated the optical properties of SnO_2/ZnO core-shell nanowires. The PL spectrum of the core SnO_2 nanowires was found to be a broad emission band which peaks at 2.1 eV around the yellow region. This yellow emission is ascribed to the trapped states within the band gap, which is formed by the interaction of oxygen vacancies with interfacial tin or dangling bonds. For the as-fabricated SnO_2/ZnO core-shell nanowires, the PL spectrum is found to be consisted with two peak positions which are located at approximately 2.1 eV and 3.2 eV, respectively. The emission band in the yellow region is assumed to originate from the SnO_2 core and the UV emission band around 3.2 eV can be associated with the excitons in ZnO shell.[100]

SnO_2 acts as both donors and acceptors[101]and its electrical conduction is owing to the existence of point defects (native and foreign atoms). SnO_2 exhibited non-linear electrical properties between current *I* and potential *V*, described by the relation $I=CV^{\alpha}$ (where C is a constant that depends on the microstructure and α is the non-linear coefficient).[102] Significant improvement in electrical properties has been observed in core-shell structures of SnO_2 nanocrystals. In the type-II interaction between the two semiconductor materials, the efficient charge separation takes place in the core-shell structure.[36] Upon photoexcitation, electrons are accumulating in the SnO_2 core whereas holes are in the semiconductor shell. As a result, SnO_2-based type-II core-shell structures can be act as a good charge storage material due to efficient charge separation. Patra et al.[36] have reported some interesting changes in electrical properties of core-shell SnO_2/CdS nanorod. Figure 3d(i) shows the I-V characteristic for pure SnO_2 and core-shell SnO_2/CdS heterostructure. They have found asymmetric and non-linear I-V characteristics for both the samples which indicate the formation of a Schottky barrier.[1] The work function value of SnO_2 is 4.5 eV, and that of Au is 5.1 eV.[1] Thus, the Au electrode is made to facilitate electron flow from the SnO_2 to the Au electrode since the Fermi level of the SnO_2 is initially higher than that of Au before the contact was made.[103] This process results in the formation of an electron depleted region at the surface of the SnO_2 that corresponds to a Schottky barrier between SnO_2 and the Au electrode. It is also observed that the conductivity is lower in the core-shell structure compared to SnO_2. It is explained with the help of a schematic model (figure 3d(ii)). The efficient charge separation occurs; electrons are accumulating in the core whereas holes are in the shell (figure 3d(ii)). Thus, carrier transport is hampered due to the barrier and thus the conductivity is decreased. Kim et al.[70] have shown that the conductivity of the pure SnO_2 nanowire is 2.76 S/cm at room temperature, whereas the conductivity of the core-shell SnO_2/In_2O_3 nanowires is 145.5 S/m, which is 2 orders of magnitude higher than that of the pure SnO_2 nanowire. The elevated conductivity of the core-shell nanowire is due to the formation of the ITO shell nanostructure caused by the successful incorporation of Sn into the In_2O_3 lattice. Archer et al.[65] reported the capacity value of core-shell SnO_2@C nanocolloids is 440 mAh/g at a current density of 300 mA/g. Park et al.[104] have reported higher PCE (2.62%) for a bilayer structure of the SnO_2 nanoparticle and ZnO nanorod. Introduction of ZnO on the SnO_2 layer improves significantly electron transport and lifetime compared to the SnO_2 film. It reveals that

the significant modification of optical and electrical properties of SnO_2 is observed by forming core-shell structures.

3.3. Photo-electrochemical properties

SnO_2 does not respond to visible light excitation because of wide band gap semiconductor (Eg = 3.6 eV)[36]. Compared with TiO_2 and ZnO, SnO_2 is a better electron acceptor since its conduction band (ECB = + 0.45 V vs NHE at pH 1) lies -0.5 V more positive than that of TiO_2 and ZnO. A wide variety of organic and organometallic molecules have already been employed to sensitize SnO_2 electrodes.[105,106] However, the suppression of the recombination of photogenerated charge carriers in SnO_2 is essential for improving the efficiency of net charge transfer at the SnO_2 electrolyte interface. A variety of approaches are considered to improve the charge separation in SnO_2 systems. Most promising one is the coupling with another semiconductor with different energy levels.[107] Recently, considerable attention[108-109] has been paid on studying SnO_2-based coupled semiconductor systems such as core-shell structured SnO_2/TiO_2[37-38], SnO_2/CdS[36], SnO_2/CdSe.[39-41,64,110] etc. Such coupled semiconductor systems not only extend the photoresponse of large band gap semiconductors but also rectify the flow of photogenerated charge carriers[39] and improve the efficiency of dye sensitization.[108] Development of such semiconductor core-shell heterostructures are also considered to be interesting by changing the thickness of the shell.

Kamat et al.[111] have reported the charge injection from an excited Ru(II) complex into SnO_2 and core-shell SnO_2/CdS to clarify the advantageous effect of core-shell semiconductor systems. The preparation of Ru(II)-modified core-shell SnO_2/CdS semiconductor films on a conducting glass electrode (OTE) is represented schematically in fig. 4a. Figure 4b illustrates the photocurrent response of OTE/SnO_2 and OTE/SnO_2/CdS electrodes before and after modification of Ru (II) complex. It is found that both OTE/SnO_2 and OTE/SnO_2/CdS electrodes upon modification with Ru(II) complex exhibits a prominent peak around 470 nm. A proposed mechanism is given for dye sensitized photocurrent generation in a core-shell semiconductor film in fig. 4c. Nasr et al.[64] have fabricated a photoelectrochemical cell with a core-shell SnO_2/CdSe nanocrystalline semiconductor electrode and it is found that the coupling of CdSe with SnO_2 leads to an improvement in the performance of OTE/SnO_2/CdSe over OTE/CdSe cells in terms of photon-to-current conversion efficiency. Sun et al.[112] have reported the optoelectronic properties of core-shell SnO_2/CdS and it is found that core-shell SnO_2/CdS shows an efficient

reply to photons in the visible region. The incident photon-to current conversion efficiency (IPCE) is up to 6.5 in the range of 400 to 440 nm. In the visible region, the IPCE observed above is higher than that of the pure SnO_2 cell. Bedja et al.[107] have effectively prepared core-shell SnO_2/TiO_2 and have showed an advanced photochromic and photocatalytic efficiencies of the as-prepared sample. The improved charge separation in this system has been substantiated by the enhanced efficiency of hole trapping monitored from the absorption peak at 360 nm. This core-shell system is useful for the oxidation of I^- and SCN^-. Vinodgopal et al.[38] have investigated the photoelectrochemical properties of the core-shell SnO_2/TiO_2 films under both nitrogen- and oxygen-saturated conditions and as a function of varying composition. Since the conduction band of SnO_2 (0 V vs NHE at pH 7) is lower than that of the TiO_2 (-0.5V vs NHE at pH 7), the former acts as a sink for the photogenerated electrons.[38] The holes move in the opposite direction from the electrons and accumulate on the TiO_2 particle, thereby making charge separation more effectively and thus enhancing the photoelectrochemical performance. Tennakone et al.[113] have fabricated a dye-sensitized photoelectrochemical cells based on porous core-shell SnO_2/ZnO and it is found that the core-shell SnO_2/ZnO cell is more stable than the TiO_2 cell. The cell made of SnO_2/ZnO is superior because of the ballistically injection of "hot carrier". The TiO_2-coated SnO_2 nanoporous electrode is being used for DSSC applications.[114] Gao et al.[72] have reported a simple procedure to prepare SnO_2/TiO_2 core-shell photoanodes for DSSCs. The power conversion efficiency (PCE) value of the SnO_2/TiO_2 core-shell is 5.11% which is five times higher than that of SnO_2 nanotube DSSCs (0.99%). This PCE value is also higher than that of TiO_2 nanoparticles (P25) DSSCs (4.82%). Tennakone et al.[115] have reported the improvement of photovoltage by a thin oxide layer coating on the surface of SnO_2 because the shell layer acts as a barrier layer against recombination due to higher conduction band edge of shell material. Core-shell SnO_2@AO (A = Ni, Cu, Zn and Mg) films were prepared and the effects of core-shell structures on photovoltaic properties are reported by Park et al.[116] They have observed that the dye-sensitized core-shell films exhibit higher performance than the bare SnO_2 film. Again, it reveals that the core-shell structure improves the photoelectrochemical property of SnO_2 due to well-organized charge separation.

3.4. Photocatalytic properties

Photocatalytic activity depends on the ability of the catalyst to create electron-hole pairs and formation of free radicals for secondary reactions. Most commonly used heterogeneous

photocatalysts are semiconductors,[117] SnO_2 particularly has attracted great attention.[33,118,119] During the photo-excitation, an electron is excited from the valance band to the conduction band, leaving behind a hole. The photogenerated electron and hole can recombine, or else the hole may react with an electron donor such as a reagent (e.g. a pollutant). However, the fast recombination rate of the photogenerated electron/hole pairs in pure SnO_2 hampers,[120] thus the core-shell structures of SnO_2 are being used to enhance the photocatalytic efficiency by increasing the charge separation and extending the photo-responding range into the visible region.

Considering the band structures of a SnO_2-based core-shell nanocatalyst,[121,122] different work functions lead to the negatively charged carriers moving from SnO_2 (the material with low work function) to other semiconductor shell material (the one with high work function) until their Fermi levels align; thus, an electrostatic field is created at the interface. At thermal equilibrium, the conduction band (CB) and valence band (VB) of SnO_2 and other semiconductor shell material bend, and a depletion layer forms around the interface. When SnO_2-based core-shell nanocatalyst is radiated by UV light with photon energy higher or equal to the band gaps of SnO_2 and other semiconductor, electrons (e^-) in the VB can be excited to the CB with simultaneous generation of the same amount of holes (h^+) in the VB. The photogenerated electrons and holes are separated under the influence of the electrostatic field induced by different work functions. Thus, electrons move to the SnO_2 side and holes to the shell side. Then, the electronic acceptors like adsorbed O_2 can easily trap the photoelectrons to produce a superoxide anion radical ($\cdot O^{2-}$).[123] The formed $\cdot O^{2-}$ might either attack organic molecules or provide hydroxyl radical species ($\cdot$OH) by reacting with photogenerated electrons.[124] The photoinduced holes can be easily trapped by OH^- to further produce a $\cdot$OH species, which is an extremely strong oxidant for the partial or complete mineralization of organic chemicals.

There are a number of studies related to the photocatalytic activity of core-shell SnO_2 such as SnO_2/TiO_2[63,125], SnO_2/ZnO[126,127], SnO_2/CdS[36] etc. Zheng et al.[127] have proposed a band structure model of the SnO_2/ZnO heterojunction nanocatalyst (figure 5). From the proposed band structure model, it is seen the core-shell SnO_2/ZnO exhibits higher photocatalytic activity than pure SnO_2 and ZnO. Wang et al.[128] have fabricated core-shell SnO_2/Fe_2O_3 heterostructures by a low-cost and environmentally friendly hydrothermal strategy. The as-fabricated SnO_2/Fe_2O_3 exhibits excellent visible light or UV photocatalytic abilities mainly owing to the effective electron-hole separation at the SnO_2/Fe_2O_3 interfaces. Pan et al.[63] have investigated the

photocatalytic behavior of core-shell SnO_2/TiO_2 nanowire by decomposition of methyl violet under UV illumination. Figure 6a summarizes the results of the photocatalytic activity of pure SnO_2 nanowire and core-shell SnO_2/TiO_2 nanowire. The degradation rate of methyl violet was found to be 4.3% for pure SnO_2 nanowire which was enhanced to 95.6% in core-shell structures. The enhanced photocatalytic activity in core-shell nanowire is attributable to higher surface area and the change in the electronic structures caused by Sn^{4+} doping in TiO_2. The photocatalytic behavior of the core-shell SnO_2/V_2O_5 nanowires for the photodegradation of toluidine blue "O" dye (TBO) under UV exposure was examined.[69] The significant improvement of the photocatalytic activity of the core-shell SnO_2/V_2O_5 nanowires is attributed mostly to its large specific surface area and efficient charge separation at the core-shell SnO_2/V_2O_5 photocatalyst interface. It is demonstrated that photogenerated electron occurs from the conduction band of SnO_2 which is then injected into the lower lying conduction band of V_2O_5, during the photoexcitation of SnO_2/V_2O_5 nanowires. The photogenerated holes in the V_2O_5 valence band are transferred to the valence band of SnO_2, which increase the spatial separation of the charge carriers, thereby reduces the probability of recombination relative to that of interfacial charge transfer. Shao et al.[129] have investigated the photocatalytic activity of core-shell SnO_2/ZnO nanofibers which is higher than the pure ZnO and SnO_2 nanofibers due to the formation of SnO_2-ZnO heterojunction which could improve the separation of photogenerated electrons and holes. Liu et al.[68] have reported the photocatalytic properties of core-shell SnO_2/TiO_2 nanofibers and it reveals that the core-shell SnO_2/TiO_2 nanofibers exhibit enhanced photocatalytic efficiency. The band gap of anatase TiO_2 and rutile SnO_2 is 3.2 and 3.6 eV respectively; the work function of TiO_2 is around 4.2 eV, its electron affinity is about 4.2 eV; the work function of SnO_2 is around 4.4 eV, its electron affinity is about 0.5 eV larger than that of TiO_2.[68] Accordingly, a Type II heterojunction is formed in the SnO_2/TiO_2 interface. The Fermi energy level of TiO_2 is higher than that of SnO_2 because of its smaller work function, so that electron transfer occurs from the conduction band of light activated TiO_2 to the conduction band of light activated SnO_2 and, conversely, hole transfer occurs from the valence band of SnO_2 to the valence band of TiO_2. The efficient charge separation increases the lifetime of the charge carriers and enhances the efficiency of the interfacial charge transfer to adsorbed substrates. Kar et al.[36] have reported the photodecomposition of Congo red dye under UV irradiation for pure SnO_2 nanorod and core-shell SnO_2/CdS nanorod. Figure 6b illustrates the Congo red decomposition rate as a function of

UV irradiation time. Pure SnO_2 nanorod and core-shell SnO_2/CdS nanorod is checked for 240 min under identical conditions. It is found that 97% of Congo red dye is degraded by core-shell SnO_2/CdS nanorod after 240 min UV irradiation, whereas, only 20% degradation is found for pure SnO_2 nanorod. Core-shell SnO_2/CdS nanorod enhances the separation of photogenerated electron-hole pairs due to the potential energy differences between SnO_2 and CdS, which increases the photocatalytic activity. Vinodgopal et al.[38] have demonstrated the photocatalytic activity of core-shell SnO_2/TiO_2 in degradation of textile azo dye. Peng et al.[34] have synthesized core-shell SnO_2/TiO_2 nanotubes and found the enhanced photocatalytic property in the core-shell sample. The photocatalytic activity of the core-shell SnO_2/TiO_2 nanotubes is found to be increased with increasing SnO_2 content. A schematic diagram of the charge transfer process in the core-shell SnO_2/TiO_2 nanotubes photocatalysts is given to understand the mechanism (figure 6c). In core-shell SnO_2/TiO_2, the absorption of a photon by TiO_2 nanotubes leads the promotion of an electron from the valence band to the conduction band of TiO_2 nanotubes and then the electron is transferred to the conduction of SnO_2 i.e. the conduction band of SnO_2 acts as a sink for photogenerated electrons. While the photogenerated holes moves in the reverse direction, they accumulate in the valence band of the TiO_2 nanotubes, which enhances the efficiency of charge separation. Melghit et al.[35] have found that the Congo red photo-degradation increases when a core-shell sample is being used. The as-synthesized core-shell SnO_2/SnS_2 nanosheets show enhanced visible light photocatalytic activity, which is extraordinarily superior from the pure SnS_2 and SnO_2.[86] This discussion clearly reveals that the core-shell structure improves the photocatalytic activity of SnO_2 due to efficient charge separation.

3.5. Gas sensing properties

In principle, gas sensing by semiconducting metal oxide is based on the oxidation-reduction reaction of the detected gases going on the semiconductor surface, which causes a significant resistance change in proportion to the gas concentration.[130,131] For a given type of material, the sensor performance depends on various factors such as the working temperature, exposed crystal planes, grain size, doping or surface modification, and so on.

Among the different semiconducting metal oxides, SnO_2 gas sensor was initially proposed[132] and patented in 1962.[133] SnO_2 is one of the most significant material for use as gas sensor for domestic, commercial and industrial purposes due to its low operating temperatures, high sensitivities, mechanical simplicity and low manufacturing costs.[134,135] Extensive research

has been conducted on understanding the chemical and electronic mechanisms that preside over SnO_2 sensor performance and on extending SnO_2 sensors to detection of other gases, including trace amounts of toxic gases.[136,137] Unfortunately, lot of difficulties exists with SnO_2 sensors and this is typically due to low surface area and low stability. SnO_2 sensors often provide an undesired signal when an inert gas is present in the environment. SnO_2 sensors also tend to lack long-term stability and require a moderately high operating temperature. SnO_2-based sensors also involve long response and recovery times. One fashionable way to overcome these problems is to construct various SnO_2-based core-shell heterostructures.

For SnO_2, the sensing mechanism is typically explained by the space-charge model.[138] In this model, the sensitivity of SnO_2 is strongly dependent on the change of the space-charge length under different gas atmospheres, resulting in higher sensitivity of the sensing materials with smaller size.[139] However, the electron transport mechanism of the core-shell heterostructures should be significantly different from that of the pure SnO_2 and other shell material due to the formation of heterojunctions at their interfaces. Electron transport is thus expected to be strongly tuned by the heterojunction barrier. Jin et al.[140] have presented energy band structures [figure 7(i)] for as-synthesized core-shell SnO_2/Fe_2O_3 heterostructures. The band gaps of SnO_2 and Fe_2O_3 at room temperature are 3.6 eV[1] and 2.1 eV. Thus the energy band structure of the SnO_2/Fe_2O_3 heterojunction is schematically depicted in figure 7(i), where φ_{eff} denotes the effective barrier height considering the contribution of other factors such as temperature to the barrier height. Therefore, it requires that the transport of electrons should overcome the heterojunction barriers.[141] The φ_{eff} will increase in air because electrons are trapped both in SnO_2 and Fe_2O_3 induced by adsorbed oxygen species as shown in figure 7(i). When the core-shell heterostructures are exposed to ethanol vapor, the reaction between the adsorbed oxygen species and the ethanol molecules leads to the release of the trapped electrons back simultaneously into the conduction bands of the SnO_2 and Fe_2O_3, resulting in a decrease in the width and height of the barrier potential at their interfaces [figure 7(i)]. Thus, the conductivity of the heterojunction will consequently be significantly increased and as a result high sensitivity of the SnO_2/ Fe_2O_3 heterojunctions to ethanol is observed. Xue et al.[142] have fabricated core-shell PN-junction nanorods using N-type SnO_2 coated with P-type CuO which is extremely high sensitivity against H_2S at room temperature. They have proposed an energy band diagram which is shown in figure 7(ii) to describe the response and recovery process of core-shell CuO-SnO_2

PN-junction nanorod sensors against H_2S. In air, the barriers at the PN-junctions greatly block the electrons transporting through the nanorods. After putting the sensors in H_2S, the CuO nanoparticles are converted to CuS nanoparitcles by the following chemical reaction:[143]

$$CuO + H_2S = CuS + H_2O \quad (1)$$

Since the work function of metallic CuS is lower than that of SnO_2, the band bends downward and no barrier exists between them, which makes for easy flow of the electrons. Thus, the resistance of the sensors in H_2S is much lower than that in air. Chen et al.[144] have productively prepared core-shell SnO_2/Fe_2O_3 heterostructures which exhibits a dramatic improvement in ethanol sensing characteristics including strong sensor response, low working temperature and a good selectivity. Here, the heterojunction barrier and the contact barrier are influenced by the adsorption and desorption of oxygen species which control the electron transport in the core-shell nanorods. Liu et al.[145] have synthesized core-shell SnO_2/Fe_2O_3 nanotubes and studied the toluene sensing properties. Their results revealed that the optimum operating temperature to detect toluene is 260°C, the lowest detecting limit to toluene is 50 ppb, and the response value is 2.0. Gao et al.[59] have successfully prepared core-shell SnO_2/CdS heterostructures with high gas sensing properties. Their results are depicted in figure 8a which shows the characteristic response curves of the SnO_2 sensors and the core-shell SnO_2/CdS sensors. The jump of the conductance is due to the variation of carrier density in the SnO_2 that relates to the absorption-desorption of oxygen. From fig. 6a, an improved ethanol-sensing performance of the core-shell sample is observed. Considering the efficient charge separation in SnO_2/CdS core-shell heterostructures, it is suggested that the CdS shell would be served as additional electron source which significantly improve the electron conduction in SnO_2. The SnO_2-In_2O_3 core-shell system exhibits significantly higher gas sensitivities than pure SnO2.[66] The In_2O_3 shell provided improved sensor performance via electronic interaction with the SnO_2. Jia et al.[31] have synthesized a hierarchically arrangement of core-shell SnO_2/ZnO for gas sensing applications. A favorable response to ethanol vapor even at a very low concentration of 10 ppm is monitored. They demonstrated that the detection limit of core-shell SnO_2/ZnO sensor is in the range of 10 to 100 ppm of ethanol with timely response and recovery. The improved gas sensitivity of core-shell SnO_2/ZnO sensor is attributed to the larger grain size, porosity and active surface state which would allow the test gases to be adsorbed on its surface. Wang et al.[146] have developed an innovative model for a chemical sensor which is Au nanoparticle-decorated porous SnO_2 hollow

spheres. Their model exhibits outstanding sensing performances by using ethanol as a probe molecule. The improved sensing features are attributable to the improved gas diffusion and mass transport induced by the unique porous structure. Choi et al.[32] have investigated the gas sensing properties of core-shell SnO_2/ZnO nanofibers. They have measured the dynamic performance of core-shell SnO_2/ZnO nanofiber sensor to O_2 and NO_2 gas. It is found that the resistance of the sensor increases upon exposure to O_2, while it decreases upon the exclusion of O_2. The better sensitivity of the core-shell nanofiber sensor is attributed to the change in resistance due to both the surface depletion layer of each core-shell nanofiber and the potential barriers built in the junctions caused by the combination of homo- and hetero-interfaces. Zhang et al.[58] have examined the gas sensing properties of rattle-type SnO_2/SnO_2 core-shell structure and the results are illustrated in figure 8b. Figure 8b (i) illustrate the response of solid, hollow and rattle-type SnO_2 sensors to ethanol under an operating temperature of 300^oC. They have observed 6.4 times elevated gas response for the rattle-type core-shell nanospheres compared to solid nanospheres. Figure 8b (ii). Figure 8b (iii) represents the responses of solid, hollow and rattle-type SnO_2 nanospheres to 50 ppm of C_2H_5OH, H_2 and CO. The enhanced ethanol sensing characteristics of rattle-type SnO_2 nanospheres are mainly attributed to different morphologies, i.e., perfect rattle-type structure and hollow structures. They have stated that the effective contact surface area will increase and the amount of target gas absorbed onto the surface of materials. Wu et al.[67] have synthesized polypyrrole-coated SnO_2 hollow spheres core-shell hybrid materials and found that the core-shell hybrid acquire very fast response and enhanced sensitivity to ammonia gas at room temperature. This core-shell hybrid sensor shows almost a linear response to NH_3 concentration which implies that the as-prepared core-shell hybrids are of great potential value for gas sensor applications. They have suggested that the SnO_2 hollow spheres are enwrapped and interconnected with polypyrrole coatings, which could be an excellent pathway for electron transfer in the gas sensing process. Core-shell SnO_2/Fe_2O_3 have been synthesized by Rumyantseva et al.[147] and the high sensitivity is ascribed to its high specific surface area and reduced grain size. Ga_2O_3/SnO_2 core-shell nanowires[148] sensor showed an order of magnitude higher gas response toward ethanol against other gases, such as H_2, CO, and NH_3. Yu et al.[149] have developed SnO_2 nanotubes loaded with Ag_2O nanoparticles to improve gas sensing performance towards ethanol and butanone. The enhanced gas sensing behavior is attributed to the improvement of surface reactions involving adsorption, dissociation and the ionization of

oxygen by the occurrence of Ag_2O. The above discussion ascertains that the gas sensing property of SnO_2 is significantly influenced by core-shell structures.

4. Summary and perspectives

This study undoubtedly demonstrates that the core-shell SnO_2 nanocrystals could pave the way for developing new challenging devices because core-shell structures improve different physical properties e.g. electrical, optical, and electrochemical etc. Novel building blocks can be produced for applications in the areas of solar cells, catalytic support materials, transparent electrodes and solid-state chemical sensors. The significance of these finding goes away from the basic science of core-shell SnO_2 nanocrystals and it is found to be given impact on diverse applications in optical, electrical, gas sensing, photocatalytic and photo-electrochemical. The development of SnO_2 nanocrystals-graphene composites may offer an imperative landmark for the applications in light energy harvesting and solar cells. The design of innovative optical-based materials based on conjugated polymer nanoparticle-SnO_2 nanocrystals will provide new possibilities for optoelectronic applications. Although quite a lot of matters are to be addressed, the broad interest in SnO_2-based applications is predictable to develop in the coming years because applications are still in the developing period. Consequently, further investigations in this field are essential for exhaustively understanding of the phenomenon.

Acknowledgements

"DAE-SRC Outstanding Investigator Award" is acknowledged for financial support. Special thanks to Mr Gopal Krishna Manna, IACS for graphic design.

References

1 A. Kar and A. Patra, *J. Phys. Chem C*, 2009, **113**, 4375.

2 X. Xu, J. Zhuang and X. Wang, *J. Am. Chem. Soc.,* 2008, **130**, 12527.

3 A. Kar and A. Patra, *Trans. Ind. Ceram. Soc.*, 2013, **72**, 89.

4 P. G. Harrison and M. J. Willet, *Nature,* 1988, **332**, 337.

5 S. Ferrere, A. Zaban and B. A. Gregg, *J. Phys. Chem. B*, 1997, **101**, 4490.

6 W. W. Wang, Y. J. Zhu and L. X. Yang, *Adv. Funct. Mater.*, 2007, **17**, 50.

7 J. Zhu, Z. Lu, S. T. Aruna, D. Aurbach and A. Gedanken, *Chem. Mater.*, 2000, **12**, 2557.

8 Y. S. He, J. C. Campbell, R. C. Murphy, M. F. Arendt and J. S. Swinnea, *J. Mater. Res.*, 1993, **8**, 3131.

9 Y. Wang, X. Jiang and Y. Xia, *J. Am. Chem. Soc.*, 2003, **125**, 16176.

10 G. Xi and J. Ye, *Inorg. Chem.*, 2010, **49**, 2302.

11 S. Sain, A. Kar, A. Patra and S. K. Pradhan, *CrystEngComm*, 2014, **16**, 1079.

12 Z. Liu, D. Zhang, S. Han, C. Li, T. Tang, W. Jin, X. Liu and C. Zhou, *Adv. Mater.*, 2003, **15**, 1754.

13 A. Kolmakov, D. O. Klenov, Y. Lilach, S. Stemmer and M. Moskouits, *Nano Lett.*, 2005, **5**, 667.

14 T. Seeger, P. K. Redlich and M. R. Uhle, *Adv. Mater.*, 2000, **12**, 279.

15 J. Hu, Y. Bando, Q. Liu and D. Golberg, *Adv. Funct. Mater.*, 2003, **13**, 493.

16 S. S. Chang, C. W. Shih, C. D. Chen, W. C. Lai and C. R. Wang, *Langmuir*, 1999, **9**, 1819.

17 R. S. Wagner and W. C. Ellis, *Appl. Phys. Lett.*, 1964, **4**, 89.

18 P. S. Chowdhury, S. Saha and A. Patra, *Sol. State Commu.*, 2004, **131**, 785.

19 B. Cheng, J. M. Russel, W. Shi, L. Zhang and E. T. Samulski, *J. Am. Chem. Soc.*, 2004, **126**, 5972.

20 H. Zhu, D. Yang, G. Yu, H. Zhang and K. Yao, *Nanotechnol.,* 2006, **17**, 2386.

21 D. F. Zhang, L. D. Sun, J. L. Yin and C. H. Yan, *Adv. Mater.*, 2003, **15**, 1022.

22 H. G. Yang and H. C. Zeng, *Angew. Chem., Int. Ed.*, 2004, **43**, 5930.

23 G. Pang, S. Chen, Y. Koltypin, A. Zaban, S. Feng and A. Gedanken, *Nano Lett.*, 2001, **1**, 723.

24 F. Gu, S. Wang, H. Cao and C. Li, *Nanotechnol.*, 2008, **19**, 095708.

25 Z. R. Dai, Z. W. Pan and Z. L. Wang, *J. Am. Chem. Soc.*, 2002, **124**, 8673.

26 H. Ohgi, T. Maeda, E. Hosono, S. Fujihara and H. Imai, *Cryst. Growth. Des.*, 2005, **5**, 1079.

27 X. L. Ma, Y. Li and Y. L. Zhu, *Chem. Phys. Lett.*, 2003, **376**, 794.

28 Z. R. Dai, J. L. Gole, J. D. Stout and Z. L. Wang, *J. Phys. Chem. B*, 2002, **106**, 1274.

29 M. D'Arienzo, L. Armelao, A. Cacciamani, C. M. Mari, S. Polizzi, R. Ruffo, R. Scotti, A. Testino, L. Wahba and F. Morazzoni, *Chem. Mater.*, 2010, **22**, 4083.

30 Q. Wan and T. H. Wang, *Chem. Commun.*, 2005, 3841.

31 X. Jia, H. Fan, L. Qin and C. Yang, *J. Dispersion Sci. Technol.*, 2010, **31**,1405.

32 S. W. Choi, J. Y. Park and S. S. Kim, *Nanotechnol.*, 2009, **20**, 465603.

33 S. Wu, H. Cao, S. Yin, X. Liu and X. Zhang, *J. Phys. Chem. C*, 2009, **113**, 17893.

34 L. R. Hou, C. Z. Yuan and Y. Peng, *J. Hazard. Mater.* B, 2007, **139**, 310.

35 K. Melghit, M. S. Al-Rubaei and I. Al-Amri, *J. Photochem. Photobio. A: Chem.*, 2006, **181**, 137.

36 A. Kar, S. Kundu and A. Patra, *RSC Adv.*, 2012, **2**, 10222.

37 K. Vinodgopal and P. V. Kamat, *Environ. Sci. Technol.*, 1995, **29**, 841.

38 K. Vinodgopal, I. Bedja and P. V. Kamat, *Chem. Mater.*, 1996, **8**, 2180.

39 D. Liu and P. V. Kamat, *J. Phys. Chem.*, 1993, **97**, 10769.

40 R. Vogel, P. Hoyer and H. Weller, *J. Phys. Chem.*, 1994, **98**, 3183.

41 H. Matsumoto, T. Matsunaga, T. Sakata, H. Mori and H. Yoneyama, *Langmuir*, 1995, **11**, 4283.

42 N. Barsan, M. Schweizer-Berberich and W. Göpel, *Fresenius J. Anal. Chem.*, 1999, **365**, 287.

43 X. Ma, *J. Nanoeng. Nanomanuf.*, 2012, **2**, 143.

44 M. Batzill, *Sensors*, 2006, **6**, 1345.

45 I. Ortmans, C. Moucheron and A. K. Mesmaeker, *Coord. Chem. Rev.,* 1998, **168**, 233.

46 J. Pan, H. Shen and S. Mathur, *J. Nanotechnol.*, 2012, **2012**, 917320(12 pages).

47 M. A. Olopade, O. E. Awe, A. M. Awobode and N. Alu, *African Rev. Phys.*, 2012, **7**, 177.

48 H. Wang and A. L. Rogach, *Chem. Mater.*, 2014, **26**, 123.

49 R. Ghosh Chaudhuri and S. Paria, *Chem. Rev.*, 2012, **112**, 2373.

50 A. Kar, A. Datta and A. Patra, *J. Mater. Chem.*, 2010, **20**, 916.

51 S. Khanchandani, S. Kundu, A. Patra and A. K. Ganguli, *J. Phys. Chem. C*, 2013, **117**, 5558.

52 H. Kim, M. Achermann, L. P. Balet, J. A. Hollingsworth and V. I. Klimov, *J. Am. Chem. Soc.*, 2005, **127**, 544.

53 Y. Kobayashi, M. Horie, M. Konno, B. Rodríguez-GonzaLez and L. M. Liz-Marzan, *J. Phys. Chem. B*, 2003, **107**, 7420.

54 L. Wang, J. Luo, Q. Fan, M. Suzuki, I. S. Suzuki, M. H. Engelhard, Y. Lin, N. Kim, J. Q. Wang and C. J. Zhong, *J. Phys. Chem. B*, 2005, **109**, 21593.

55 F. Bao, J. F. Li, B. Ren, J. L. Yao, R. A. Gu and Z. Q. Tian, *J. Phys. Chem. C*, 2008, **112**, 345.

56 L. Carbone and P. D. Cozzoli, *Nano Today*, 2010, **5**, 449.

57 C. Cheng, B. Liu, H. Yang, W. Zhou, L. Sun, R. Chen, S. F. Yu, J. Zhang, H. Gong, H. Sun and H. J. Fan, *ACS Nano*, 2009, **3**, 3069.

58 L. Wang, T. Fei, J. Deng, Z. Lou, R. Wang and T. Zhang, *J. Mater. Chem.*, 2012, **22**, 18111.

59 T. Gao and T. Wang, *Chem. Commun.*, 2004, 2558.

60 R. Kennedy, I. Martini, G. Hartland and P. V. Kamat, *Proc. Indian Acad. Sci. (Chem. Sci.)*, 1997, **109**, 497.

61 Y. Yin and A. P. Alivisatos, *Nature*, 2005, **437**, 664.

62 X. Meng, F. Wu and J. Li, *J. Phys. Chem. C*, 2011, **115**, 7225.

63 J. Pan, S. Heuhne, H. Shen, L. Xiao, P. Born, W. Mader and S. Mathur, *J. Phys. Chem. C*, 2011, **115**, 17265.

64 C. Nasr, P. V. Kamat and S. Hotchandani, *J. Electroanal. Chem.*, 1997, **420**, 201.

65 X. W. Lou, J. S. Chen, P. Chen and L. A. Archer, *Chem. Mater.*, 2009, **21**, 2868.

66 J. T. McCue and J. Y. Ying, *Chem. Mater.*, 2007, **19**, 1009.

67 J. Zhang, S. Wang, M. Xu, Y. Wang, H. Xia, S. Zhang, X. Guo and S. Wu, *J. Phys. Chem. C*, 2009, **113**, 1662.

68 C. Wang, C. Shao, X. Zhang and Y. Liu, *Inorg. Chem.*, 2009, **48**, 7261.

69 M. Shahid, I. Shakir, S. Yang and D. J. Kang, *Mater. Chem. Phys.*, 2010, **124**, 619.

70 D. Kim, I. Hwang, S. J. Kwon, H. Kang, K. Park, Y. Choi, K. Choi and J. Park, *Nano Lett.*, 2007, **7**, 3041.

71 X. Xue, B. He, S. Yuan, L. Xing, Z. Chen and C. Ma, *Nanotechnol.,* 2011, **22**, 395702.

72 C. Gao, X. Li, B. Lu, L. Chen, Y. Wang, F. Teng, J. Wang, Z. Zhang, X. Pana and E. Xie, *Nanoscale*, 2012, **4**, 3475.

73 X. Wu, S. Zhang, L. Wang, Z. Du, H. Fang, Y. Ling and Z. Huang, *J. Mater. Chem.*, 2012, **22**, 11151.

74 X. Xue, Z. Chen, L. Xing, S. Yuana and Y. Chen, *Chem. Commun.*, 2011, **47**, 5205.

75 Z. Gu, L. Zou, Z. Fang, W. Zhu and X. Zhong, *Nanotechnol.*, 2008, **19**, 135604.

76 X. Peng, M. C. Schlamp, A. V. Kadavanich and A. P. Alivisatos, *J. Am. Chem. Soc.*, 1997, **119**, 7019.

77 R. Xie, U. Kolb, J. Li, T. Basch and A. Mews, *J. Am. Chem. Soc.*, 2005, **127**, 7480.

78 D. V. Talapin, A. L. Rogach, A. Kornowski, M. Haase and H. Weller, *Nano Lett.*, 2001, **1**, 207.

79 A. Kar and A. Patra, *Nanoscale*, 2012, **4**, 3608.

80 F. C. Hoener, A. A. Kristi, A. J. Bard, A. Campion, M. A. Fox, T. E. Mallouk, S. E. Webber and J. M. White, *J. Phys. Chem*., 1992, **96,** 3812.

81 W. Chen, Y. Qiu, Y. Zhong, K. S. Wong and S. Yang, *J. Phys. Chem. A*, 2010, **114**, 3127.

82 M. Tamez Uddin, Y. Nicolas, C. Olivier, T. Toupance, L. Servant, M. M. Müller, H-J. Kleebe, J. Ziegler and W. Jaegermann, *Inorg. Chem*., 2012, **51**, 7764.

83 H. Shi, M. Zhou, D. Song, X. Pan, J. Fu, J. Zhou, S. Ma and T. Wang, *Ceramics International*, 2014, (http://dx.doi.org/10.1016/j.ceramint.2014.02.124).

84 H. Qiao, Z. Zheng, L. Zhang and L. Xiao, *J. Mater. Sci.*, 2008, **43**, 2778.

85 S. Sun, G. Meng, G. Zhang and L. Zhang, *Cryst. Growth Des*., 2007, **7**, 1989.

86 X. Zhou, T. Zhou, J. Hu and J. Li, *CrystEngComm***,** 2012, **14,** 5627.

87 A. Kar, S. Kundu and A. Patra**,** *J. Phys. Chem. C*, 2011**, 115***,* 118.

88 P. Reiss, M. Protière and L. Li, *Small*, 2009, **5**, 154.

89 Y. Li, G. Xu, Y. L. Zhu, X. L. Ma and H. M. Cheng, *Sol. St. Commun.*, 2007, **142**, 441.

90 H. W. Kim and S. H. Shim, *Appl. Surf. Sci.*, 2006, **253**, 510.

91 G. Blattner, C. Klingshirn and R. Helbig, *Solid State Commun.*, 1980, **33**, 341.

92 J. Jeong, S. P. Choi, C. I. Chang, D. C. Shin, J. S. Park, B. T. Lee, Y. J. Park and H. J. Song, *Solid State Commun.*, 2003, 127, 595.

93 X. J. Feng, J. Ma, F. Yang, F. Ji, F. J. Zong, C. Luan and H. L. Ma, *Solid State Commun.*, 2007, **144**, 269.

94 P. Cervantes, Q. Williams, M. Cote, O. Zakharov and M. L. Cohen, *Phys. Rev. B: Condens. Matter*, 1996, **54**, 17585.

95 K. Seo, T. Lim, S. Kim, H-L. Park and S. Ju, *Nanotechnol.*, 2010, **21**, 255201.

96 R. Konenkamp, R. C. Word and C. Schlegel, *Appl. Phys. Lett.,* 2004, **85**, 6004.

97 E. P. Domashevskaya, N. M. A. Hadia, S. V. Ryabtsev and P. V. Seredin, *Eur. Phys. J. Appl. Phys.,* 2009, **48**, 10603.

98 S. Sun, G. Meng, G. Zhang and L. Zhang, *Cryst. Growth Des.,* 2007, **7***,* 1988.

99 H. W. Kim, M. A. Kebede and H. S. Kim, *Opt. Mater.*, 2009, **31**, 1853.

100 S. W. Jung, W. I. Park, H. D. Cheong, G-C. Yi and H. M. Jang, *Appl. Phys. Lett*., 2002, **80**, 1924.

101 Z. M. Jarzebski and J. P. Marton, *J. Electrochem. Soc.*, 1976, **123**, 299.

102 S. A. Pianaro, P. R. Bueno, P. Olivi, E. Longo and J. A. Varela, *J. Mater. Sci.: Mater. Electro.*, 1998, **9**, 159.

103 M. Chen, X. Xia, Z. Wang, Y. Li, J. Li and C. Gu, *Microelectron. Eng*., 2008, **85**, 1379.

104 N. K. Huu, D-Y. Son, I-H. Jang, C-R. Lee and N-G. Park, *ACS Appl. Mater. Interfaces*, 2013, **5**, 1038.

105 T. Miyasaka, T. Watanabe, A. Fujishima and K. Honda, *J. Am. Chem. Soc.*, 1978, **100**, 6657.

106 P. V. Kamat, M. A. Fox and A. J. Fatiadi, *J. Am. Chem. Soc.*, 1984, **106**, 1191.

107 I. Bedja and P. V. Kamat, *J. Phys. Chem.*, 1995, **99**, 9182.

108 S. Hotchandani and P. V. Kamat, *Chem. Phys. Lett.,* 1992, **191**, 320.

109 S. Hotchandani and P. V. Kamat, *J. Phys. Chem.,* 1992, **96**, 6834.

110 D. Liu and P. V. Kamat, *J. Electroanal. Chem. Interfacial Electrochem.,*1993, **347**, 451.

111 C. Nasr, S. Hotchandani, W. Y. Kim, R. H. Schmehl and P. V. Kamat, *J. Phys. Chem. B*, 1997, **101**, 7480.

112 H. Sun, S. Kang and J. Mu, *J. Dispers. Sci. Technol.*, 2009, **30**, 384.

113 K. Tennakone, G. K. R. Senadeera, V. P. S. Perera, I. R. M. Kottegoda and L. A. A. De Silva, *Chem. Mater.*, 1999, **11**, 2474.

114 S. Chappel, S-G. Chen and A. Zaban, *Langmuir*, 2002**, 18***,* 3336.

115 K. M .P. Bandaranayake, M. K. Indika Senevirathna, P. M. G. M. Prasad Weligamuwa and K. Tennakone, *Coord. Chem. Rev.*, 2004, **248**, 1277.

116 C. Lee, G-W. Lee, W. Kang, D-K. Lee, M-J. Ko, K. Kim and N-G Park, *Bull. Korean Chem. Soc.*, 2010, **31**, 3093.

117 N. Serpone and A. V. Emeline, *J. Phys. Chem. Lett*., 2012, **3**, 673.

118 M. Kong, Y. Li, X. Chen, T. Tian, P. Fang, F. Zheng and X. Zhao, *J. Am. Chem. Soc.*, 2011, **133**, 16414.

119 J. L. Yang, S. J. An, W. I. Park, G. C. Yi and W. Choi, *Adv. Mater.*, 2004, **16**, 1661.

120 M. R. Hoffmann, S. T. Martin, W. Choi and D. W. Bahnemann, *Chem. Rev.*, 1995, **95**, 69.

121 Y. Zheng, C. Chen, Y. Zhan, X. Lin, Q. Zheng, K. Wei and J. Zhu, *J. Phys. Chem. C*, 2008, **112**, 10773.

122 R. Konenkamp, R. C. Word and M. Godinez, *Nanotechnol.,* 2006, **17**, 1858.

123 J. Ryu and W. Choi, *Environ. Sci. Technol.*, 2004, **38**, 2928.

124 M. A. Fox and M. T. Dulay, *Chem. Rev.*, 1993, **93**, 341.

125 C. Wang, X. Wang, B. Xu, J. Zhao, B. Mai, P. Peng, G. Sheng and J. Fu, *J. Photochem. Photobiol*. *A*, 2004, **168**, 47.

126 A. Dodd, A. McKinley, M. Saunders and T. Tsuzuki, *Nanotechnol.*, 2006, **17**, 692.

127 L. Zheng, Y. Zheng, C. Chen, Y. Zhan, X. Lin, Q. Zheng, K. Wei and J. Zhu, *Inorg. Chem.*, 2009, **48**, 1819.

128 M. Niu, F. Huang, L. Cui, P. Huang, Y. Yu and Y. Wang, *ACS Nano*, 2010, **4**, 681.

129 Z. Zhang, C. Shao, X. Li, L. Zhang, H. Xue, C. Wang and Y. Liu, *J. Phys. Chem. C*, 2010, **114***,* 7920.

130 G. W. Ho, *Sci*. *Adv. Mater.*, 2011, **3**, 150.

131 N. Yamazoe, *Sens. Actuators B*, 2005, **108**, 2.

132 T. Seiyama, A. Kato, K. Fujiishi and M. Nagatani, *Anal. Chem.*, 1962, **34**, 1502.

133 K. Ihokura and J. Watson, CRC Press, Boca Raton, FL, 1994.

134 N. Yamazoe, *Sens. Actuators B*, 1992, **6**, 9.

135 V. M. Jimenez, A. R. Gonzalez-Elipe, J. P. Espinos, A. Justo and A. Fernandez, *Sens. Actuators B*, 1996, **31**, 29.

136 W. Göpel and K. D. Schierbaum, *Sens. Actuators B*, 1995, **26**, 1.

137 N. Yamazoe, *Sens. Actuators B*, 1991, **5**, 7.

138 Y. J. Chen, X. Y. Xue, Y. G. Wang and T. H. Wang, *Appl. Phys. Lett.*, 2005, **87,** 233503.

139 Y. J. Chen, X. Y. Xue, Y. G. Wang and T. H. Wang, *Appl. Phys. Lett.*, 2006 **88,** 083105.

140 Y. Chen, C. Zhu, X. Shi, M. Cao and H. Jin, *Nanotechnol*., 2008, **19**, 205603.

141 T. Weis, R. Lipperheide, U. Wille and S. Brehme, *J. Appl. Phys.*, 2002, **92,** 1411.

142 X. Xue, L. Xing, Y. Chen, S. Shi, Y. Wang and T. Wang, *J. Phys. Chem. C*, 2008, **112***,* 12157.

143 A. Chowdhuri, V. Gupta, K. Sreenivas, R. Kumar, S. Mozumdar and P. K. Patanjali, *Appl. Phys. Lett.*, 2004, **84**, 1180.

144 Y-J. Chen, C-L. Zhu, L-J. Wang, P. Gao, M-S. Cao and X-L. Shi, *Nanotechnol*., 2009, **20**, 045502.

145 H. Shan, C. Liu, L. Liu, J. Zhang, H. Li, Z. Liu, X. Zhang, X. Bo and X. Chi, *ACS Appl. Mater. Interfaces*, 2013, **5**, 6376.

146 J. Zhang, X. Liu, S. Wu, M. Xu, X. Guo and S. Wang, *J. Mater. Chem.*, 2010, **20**, 6453.

147 M. Rumyantseva, V. Kovalenko, A. Gaskov, E. Makshina, V. Yuschenko, I. Ivanova, A. Ponzoni, G. Faglia and E. Comini, *Sens. Actuators B*, 2006, **118**, 208.

148 Y-G. Jang, W-S. Kim, D-H. Kim and S-H. Hong, *J. Mater. Res*., 2011, **26**, 2322.

149 X. Chen, Z. Guo, W. Xu, H. Yao, M. Li, J. Liu, X. Huang and S. Yu, *Adv. Funct. Mater.*, 2011, **21**, 2049.

Figures Caption

Figure 1 (a) A scheme for the preparation of SnO_2/CdS heterostructure (below of the figure is the TEM image of a core-shell SnO_2/CdS heterostructure) (reprinted with permission from ref. 36, Copyright 2012, Royal Society of Chemistry). (b) Schematic illustration of the formation process of the SnO_2 rattle-type nanoreactor (below of the figure is the TEM image of a SnO_2 rattle-type nanospheres) (reprinted with permission from ref. 58, Copyright 2012, Royal Society of Chemistry).

Figure 2 (a) X-ray powder diffraction patterns of SnO_2 nanorods, CdS nanoparticles, SnO_2+CdS mixture and SnO_2/CdS heterostructure (reprinted with permission from ref. 36, Copyright 2012, Royal Society of Chemistry). (b) X-ray powder diffraction patterns of pure SnO_2 nanorods and SnO_2/CdS heterostructure (reprinted with permission from ref. 36, Copyright 2012, Royal Society of Chemistry). (c) Transmission electron microscopy (TEM) and HRTEM images of SnO_2 nanorods (i and ii) and the SnO_2/CdS heterostructure (iii and iv). The insets of (ii) and (iv) show the SAED patterns of the SnO_2 nanorods and SnO_2/CdS heterostructure. (v) and (vi) are STEM-HAADF images of a single SnO_2/CdS heterostructure nanorod. EDS elemental mapping of the spatial distribution of Sn (vii), O (viii), Cd(ix) and S (x) elements (xi) shows an STEM-HAADF image of a single SnO_2/CdS heterostructure nanorod and EDS line scans across a single SnO_2/CdS nanorod (xii–xv) for Sn, O, Cd and S elements. TEM-EDS concentration line profile of Sn, O, Cd and S, measured along the line across the length (xvi) (reprinted with permission from ref. 36, Copyright 2012, Royal Society of Chemistry).

Figure 3 (a) PL spectra of core-shell SnO_2/ZnS nanowires (i –v) under the same conditions at room temperature. The inset is the relative intensity as a function of ZnS shell treatment time (reprinted with permission from ref. 62, Copyright 2011, American Chemical Society). (b) Photoluminescence (PL) decays of SnO_2 nanorods and SnO_2/CdS heterostructures at 400 nm emission wavelength (inset plot is the corresponding PL spectrum at 295 nm) (reprinted with permission from ref. 36, Copyright 2012, Royal Society of Chemistry). (c) Schematic model proposed for different relaxation processes in SnO_2 nanorods and SnO_2/CdS heterostructure nanorods (reprinted with permission from ref. 36, Copyright 2012, Royal Society of Chemistry). (d) (i) Current vs. voltage characteristics for SnO_2 nanorods and the SnO_2/CdS heterostructure

when the voltage is applied between Au and Au terminals in a forward bias direction and (ii) schematic representation of the band gap alignment in the type-II SnO_2/CdS heterostructure to show the electron–hole separation (reprinted with permission from ref. 36, Copyright 2012, Royal Society of Chemistry).

Figure 4 (a) A scheme for the preparation of Ru(II)-Modified SnO_2/CdS composite semiconductor films on a conducting glass electrode (OTE) (reprinted with permission from ref. 111, Copyright 1997, American Chemical Society). (b) Photocurrent action spectrum of OTE/SnO_2 and OTE/SnO_2/CdS electrodes before and after modification with Ru(II) complex: (i) OTE/SnO_2 (electrolyte: 0.02 M, NaOH), (ii) OTE/SnO_2/CdS (electrolyte: 0.04 M I_2 and 0.5 M LiI in acetonitrile) (iii) OTE/SnO_2/Ru(II), and (iv) OTE/SnO_2/CdS/Ru(II) (electrolyte: 0.04 M I_2 and 0.5 M LiI in acetonitrile) (reprinted with permission from ref. 111, Copyright 1997, American Chemical Society). (c) Mechanism of dye sensitized photocurrent generation in a composite semiconductor film (reprinted with permission from ref. 111, Copyright 1997, American Chemical Society).

Figure 5 Energy-band diagram and photocatalytic mechanism of SnO_2/ZnO heterojunction nanocatalyst (vac=vacuum level; E_f=Fermi level; CB=conduction band; VB=valence band) (reprinted with permission from ref. 127, Copyright 2009, American Chemical Society).

Figure 6 (a) Comparison of the decay in absorption for SnO_2 wires, SnO_2-TiO_2 wires, SnO_2 film and TiO_2 film (reprinted with permission from ref. 63, Copyright 2011, American Chemical Society). (b) Photodegradation rate of Congo red by different photocatalysts (SnO_2 and SnO_2/CdS) under UV light irradiation for 4 h (reprinted with permission from ref. 36, Copyright 2012, Royal Society of Chemistry). (c) A schematic diagram of the charge-transfer process in the SnO_2/TiO_2 nanotubes composite photocatalysts.

Figure 7 (i) A schematic diagram of the energy band structure of the core-shell SnO_2/α-Fe_2O_3 heterostructures: (a) in air, (b) in ethanol (reprinted with permission from ref. 140, Copyright 2008, IOP publishing) and (ii) Energy band diagram of CuO-SnO_2 PN-junction nanorod sensors

showing the H_2S sensing process (reprinted with permission from ref. 142, Copyright 2008, American Chemical Society).

Figure 8 (a) Response curves of the SnO_2 nanobelt sensors and the SnO_2@CdS core-shell heterostructure sensors to 100 ppm ethanol vapors in air at a working temperature of 400^oC (reprinted with permission from ref. 59, Copyright 2004, Royal Society of Chemistry). (b) (i) Response transients of solid, hollow and rattle-type SnO_2 nanospheres to various concentrations at 300^oC (ii) gas sensing principles of solid, hollow and rattle-type SnO_2 nanospheres and (iii) responses of solid, hollow and rattle-type SnO_2 nanospheres to 50 ppm of C_2H_5OH, H_2 and CO (reprinted with permission from ref. 58, Copyright 2012, Royal Society of Chemistry).

Table 1 Different SnO_2-based core/shell heterostructures using various methods

Core/shell	Synthetic method	Basic reagent	Reference
SnO_2/C	Hydrothermal	Potassium stannate trihydrate, Glucose	65
SnO_2 /In_2O_3	Colloidal	Tin chloride hexahydrate, Indium chloride monohydrate, Ammonium hydroxide	66
SnO_2/Polypyrrole	Colloidal	Stannous chloride dehydrate, Ferric chloride, Pyrrole monomer, Glucose	67
SnO_2/TiO_2	Hydrothermal	Tin chloride pentahydrate, Titanium butyloxide, poly-vinyl pyrrolidone	68
SnO_2/V_2O_5	Hydrothermal	Tin(II) chloride, Vanadium oxytripropoxide, Ammonium metavanadate	69
SnO_2/In_2O_3	Thermal evaporation	Metallic Sn, Metallic In, Si substrate	70
SnO_2/WO_3	Colloidal	Tin(II) chloride dihydrate, Sodium tungstate dihydrate , Sodium chloride	71
SnO_2/TiO_2	Colloidal	Tin dichloride dihydrate, Titanium chloride, Polyethylene glycol, N,N-dimethyl formamide	72
SnO_2/TiO_2	Hydrothermal	Tin dichloride dihydrate, Ammonium fluoride, Ethylene glycol	73
SnO_2/MoO_3	Colloidal	Tin dichloride dihydrate, Ammonium heptamolybdate tetrahydrate, Nitric acid	74

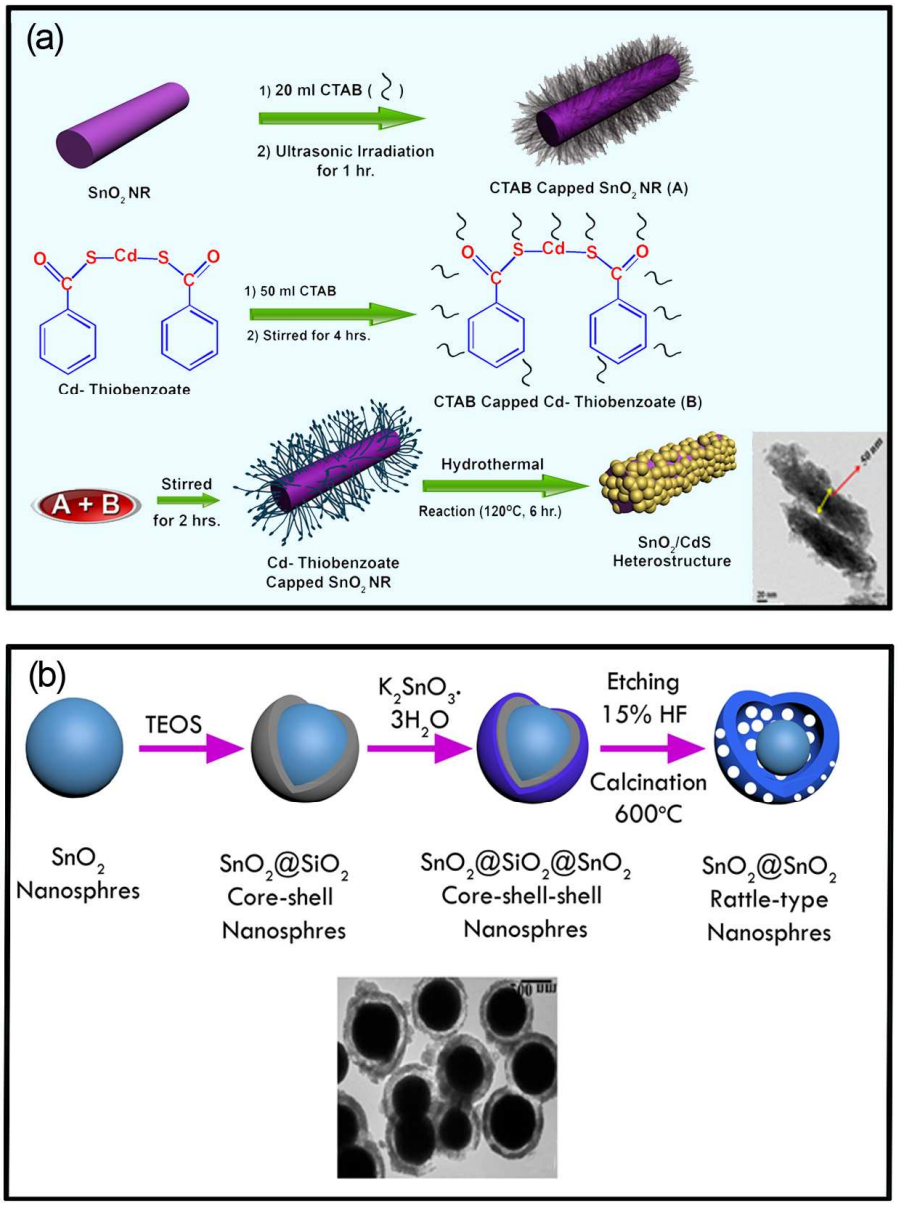

Figure 1

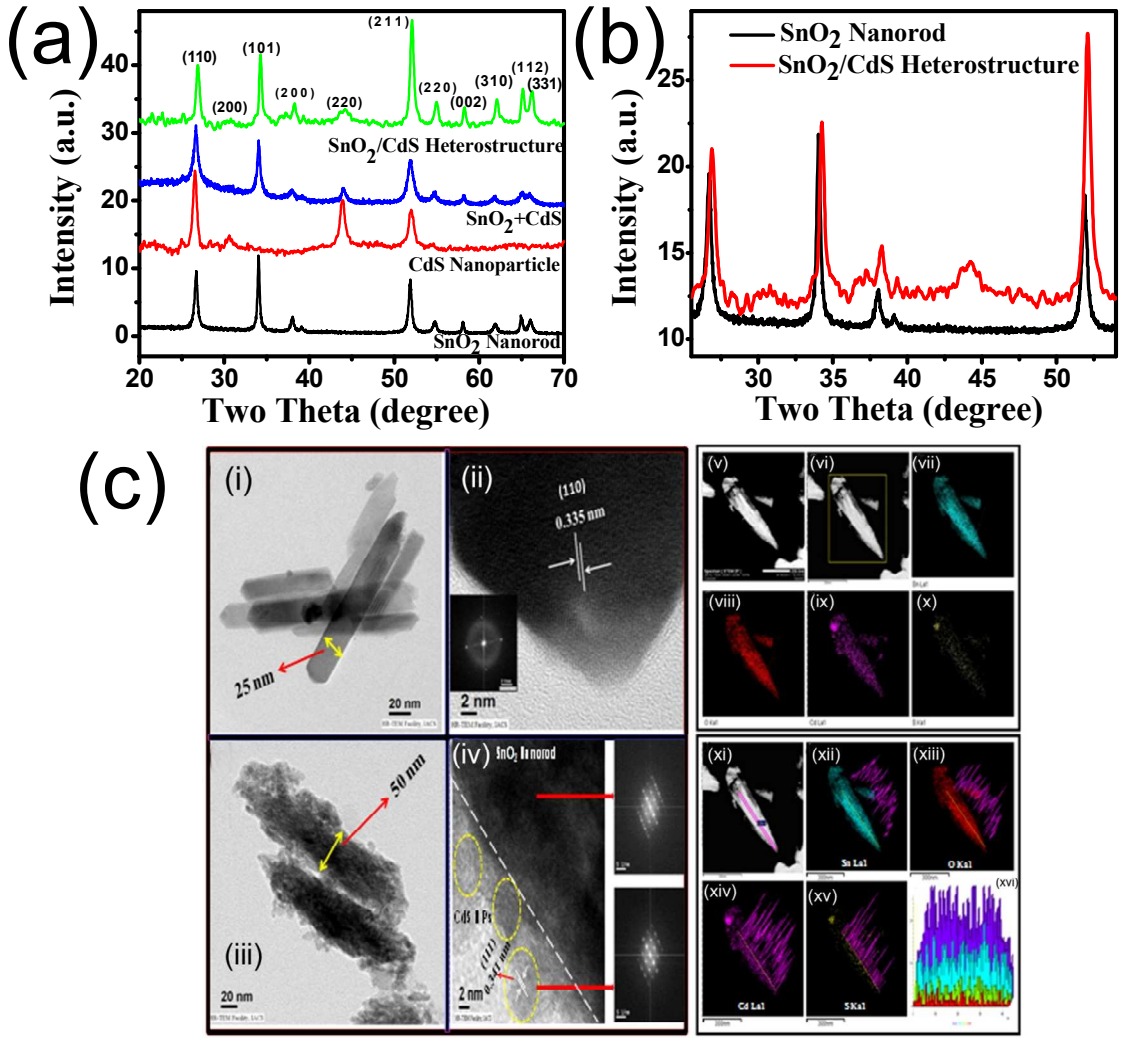

Figure 2

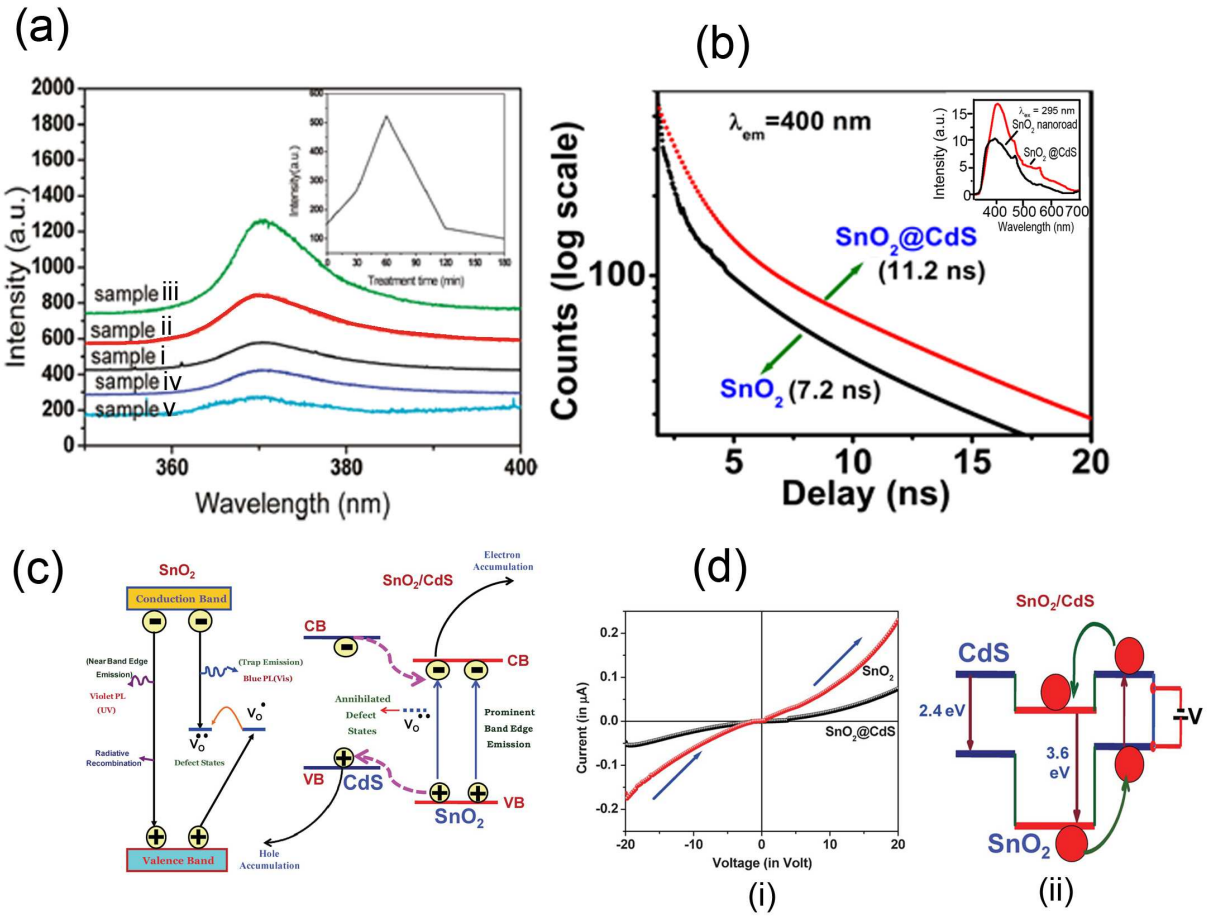

Figure 3

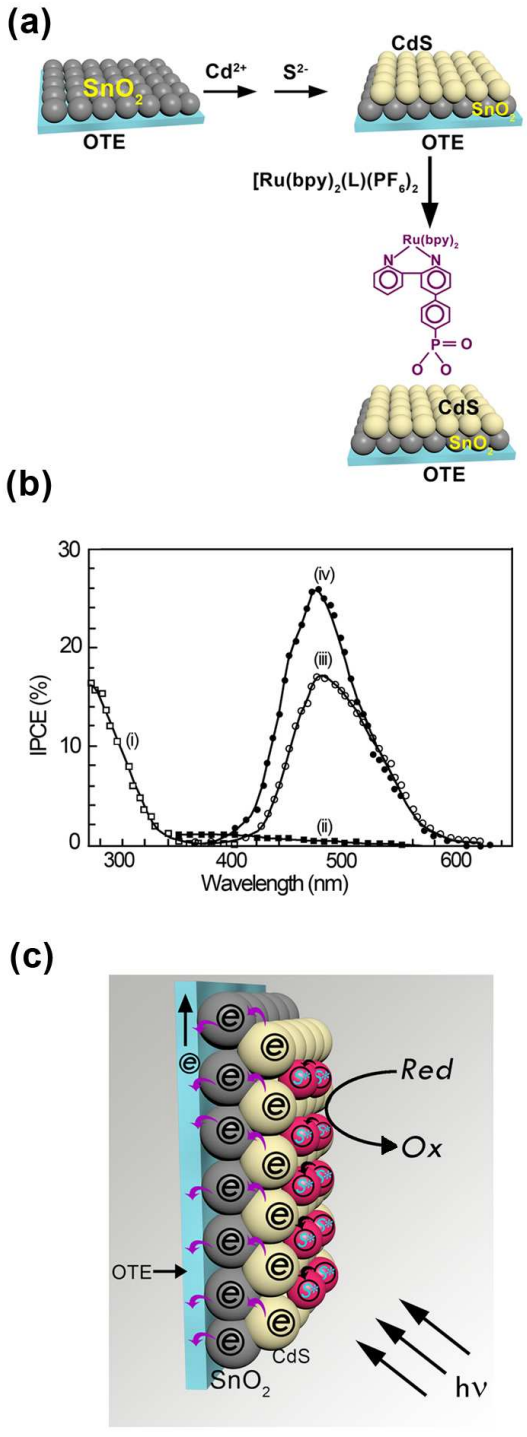

Figure 4

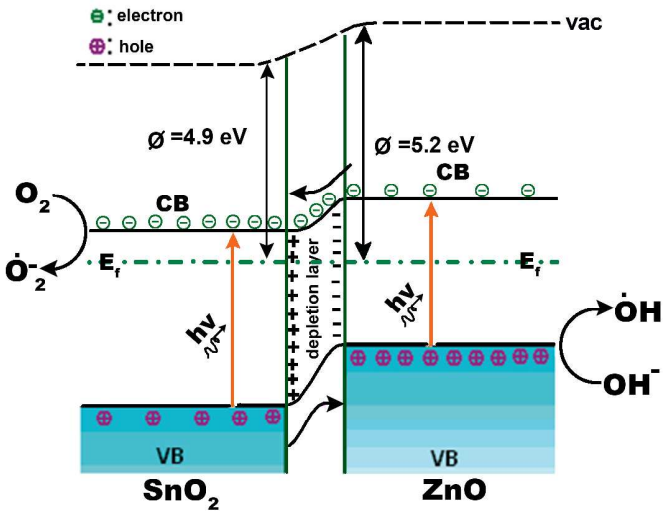

Figure 5

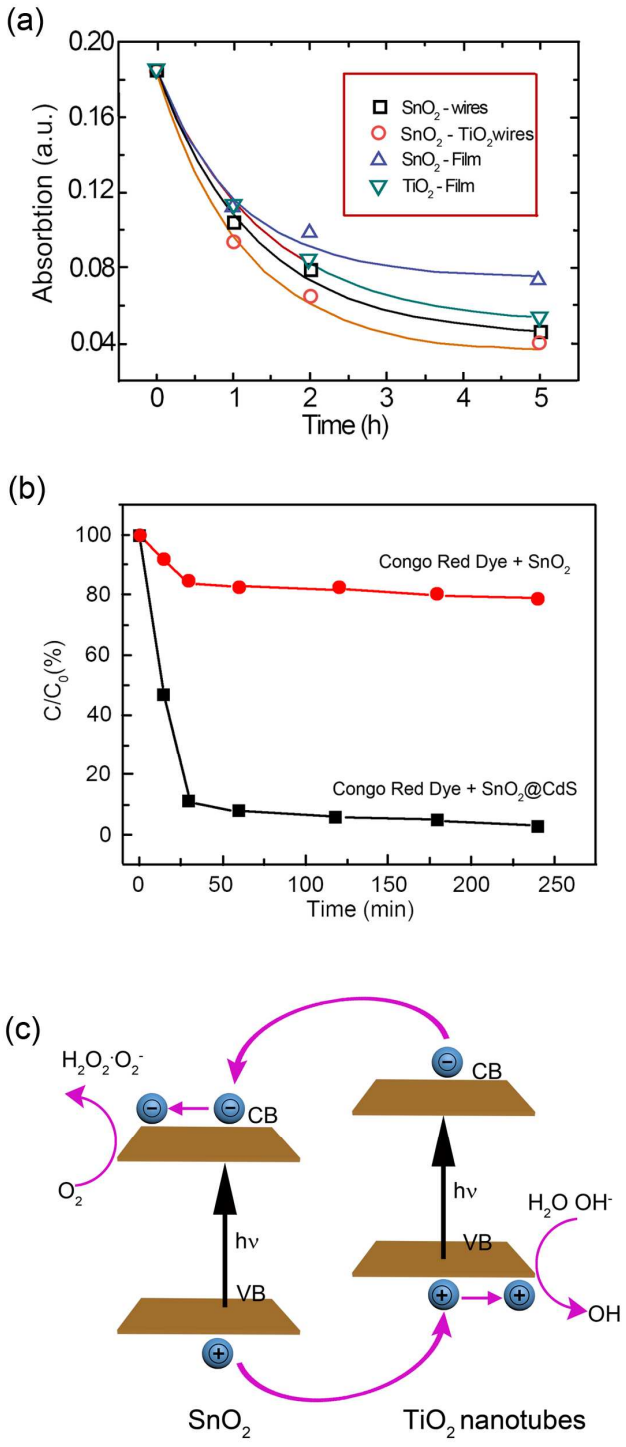

Figure 6

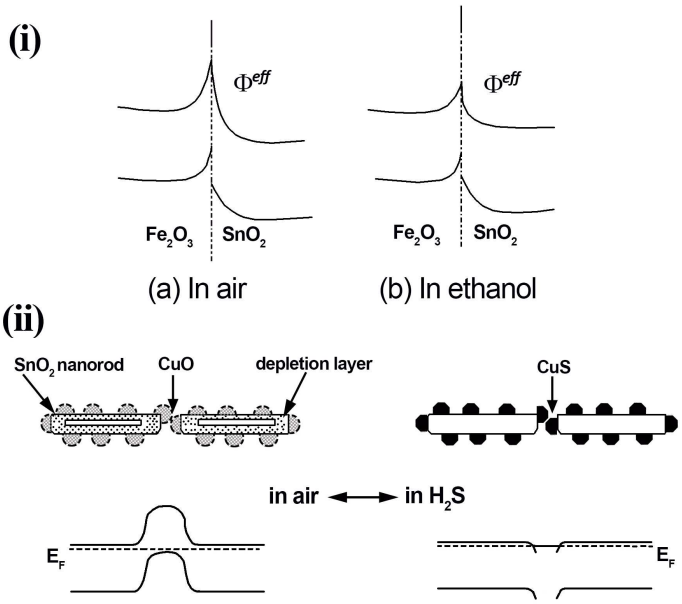

Figure 7

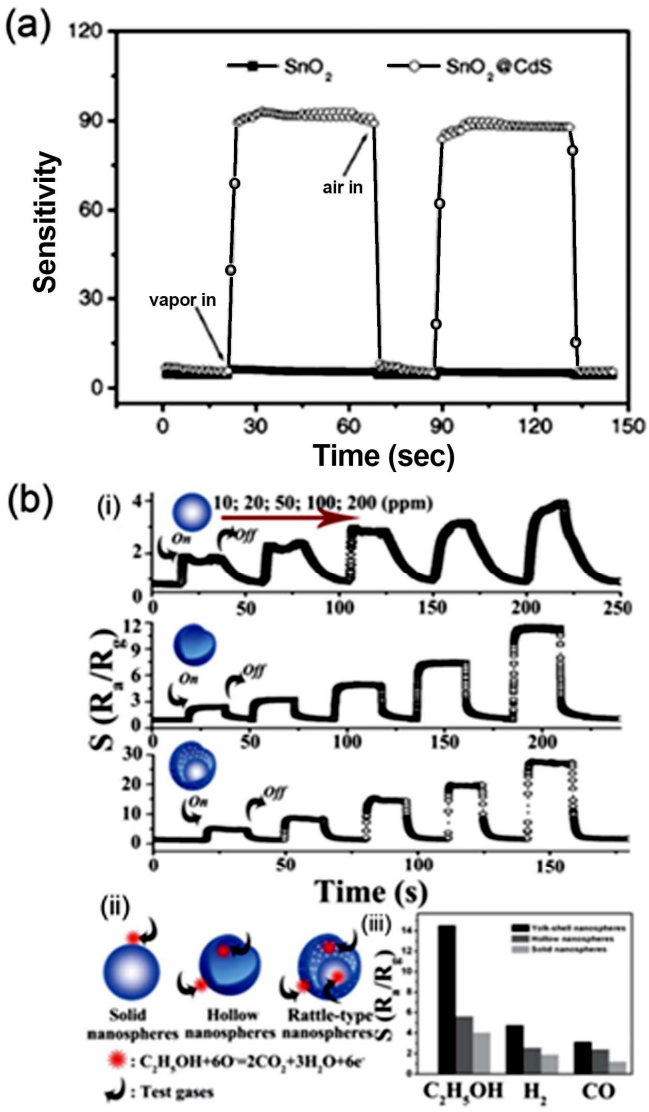

Figure 8

TOC: Core-shell structures of SnO_2 nanocrystals improve the performance of diverse applications

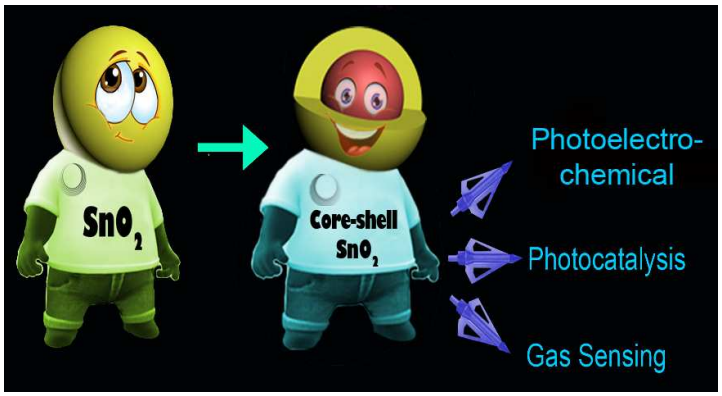

Dr. Arik Kar (born 1984) obtained his B.Sc (Hons) in chemistry from Serampore College, University of Calcutta in 2005. Later he obtained his M.Sc in chemistry from the University of Calcutta (Presidency College) with specialization in inorganic chemistry in 2007. Later he completed his Ph.D in Materials Science from Jadavpur University in 2013. He has been awarded a prestigious Royal Society's "Newton International Fellowship" for the academic year 2014-2016. He is now continuing his research as a 'Newton Fellow" in "University of Cambridge". His research interests include synthesis and characterization of different colloidal semiconductors, rare earth doped semiconductors and core-shell nanomaterials.

Prof. Amitava Patra (born 1965), received his Ph. D (1993) from Jadavpur University, India. He is now Professor at the Indian Association for the Cultivation of Science, India. He is a fellow of Royal Society of Chemistry, 2014. He is the recipient of C.N.R. Rao National Prize for Chemical Research, DAE-SRC Outstanding Investigator Award, A.V. Rama Rao Foundation Prize in Chemistry, AsiaNANO 2010 Award, CRSI Bronze Medal, Ramanujan Fellowship, MRSI Medal. He is an Advisory board member of Nanoscale and Journal of Physical Chemistry and others. He is author or co-author of more than 151 scientific papers, 3 book chapters and 2 Indian patents. His research interests include decay dynamics, energy transfer, and electron transfer of QD, Au nanoparticles, polymer and porphyrin based luminescent nanoparticles, and rare-earth based materials for up- and down- conversion luminescence.